UNITED STATES DEPARTMENT OF THE INTERIOR

GEOLOGICAL SURVEY

A Detailed Study Of The USGS Reducing-Gas Sensor With Field Tests At Long Valley, California

by

Kenneth A. McGee[1] and A. Jefferson Sutton[2]

Open-File Report 90-61

[1] David A. Johnston
Cascades Volcano Observatory
5400 MacArthur Boulevard
Vancouver, Washington 98661

[2] USGS National Center
Mail Stop 959
12201 Sunrise Valley Drive
Reston, Virginia 22092

ABSTRACT

An in-depth study of the operating characteristics of the USGS reducing-gas sensor was conducted. Sensor response to H_2S, SO_2, H_2, CO, COS, HCl, and HF was demonstrated and quantified where possible. The effects of other variables on the sensor such as temperature, pressure, load resistance, and internal resistance were measured and evaluated. Field deployment of several sensors in Long Valley caldera, California, along with analytical and meteorological studies revealed a diurnal pattern of degassing from natural sources most likely driven by solar heating and radiational cooling of the earth, though perhaps influenced by local microclimates. The control of local geologic structure on the location and extent of degassing was also demonstrated.

INTRODUCTION

Because of uplift of the resurgent dome and the occurrence of significant seismic activity, a program was begun in May 1982 to study and monitor gas emissions in and near the Long Valley caldera as a means of detecting changes that might precede tectonic or volcanic activity (McGee et al., 1982). During the past few years, several interesting degassing events have been recorded at Long Valley using USGS-made reducing-gas sensors. The relationship of these events to ongoing volcanic and tectonic processes in the area is not yet clear. In order to provide a framework in which to interpret these results as well as to answer recurring questions about the performance of the USGS reducing-gas sensor, we undertook a study that would provide data to better understand degassing phenomena and define the performance characteristics of the USGS reducing-gas sensor. The results have implications for ongoing gas studies not only at Long Valley, but also at Mount St. Helens, Hawaii, Lassen Peak, and central California, and can be used as a basis for planning further investigations.

The study is composed of both field phases and laboratory phases. The field phase, conducted in the Casa Diablo area of Long Valley caldera, was completed during August and September 1985. It was designed to test the reducing-gas sensor and its method of deployment, to verify sensor readings by independent analytical means, and to determine the effect of structure, fumaroles, and weather on degassing. The laboratory phase of the study was designed to evaluate the USGS reducing-gas sensor and test its performance under a variety of known conditions and was carried out in Vancouver, Washington.

THE USGS REDUCING GAS SENSOR

The USGS reducing-gas sensor has, at various times in the past, been referred to as the "USGS hydrogen sensor," a "fuel

cell sensor," and the "Sato sensor." Since the results of the current study indicate that the sensor responds to a variety of reducing gases including H_2, H_2S, SO_2, CO, COS, HCl, and HF, the authors feel that "reducing-gas sensor" is a more appropriate name for the sensor and will refer to it that way henceforth.

The design of the USGS reducing-gas sensor is based upon one of the most fundamental electrochemical oxidation-reduction reactions: the combination of oxygen and hydrogen to form water. The heart of the sensor is a proprietary catalytic membrane from a commercial hydrogen generator. Motoaki Sato was the first to develop a sensor based on the membrane and demonstrate its use in geochemical monitoring at Kilauea in 1973 (personal communication). He later used a similar sensor, based on the same membrane, to study the reducing capacity of fumarolic gases (including H_2 and H_2S) from Mount Baker (Malone and Frank, 1975, Sato et al, 1976).

When a DC voltage is applied across the catalytic membrane and electric current is allowed to flow in the presence of water, oxygen is released on one side of the membrane and hydrogen is released on the other. Since the reaction is reversible, the converse is also true. If hydrogen, or other fuel, is supplied to one side of the membrane, and oxygen is supplied to the other side, a current is generated that we measure as the voltage drop across a load resistor. If oxygen is present in excess, the voltage output will vary in proportion to the amount of fuel present. The sensor is thus a small battery, or fuel cell, to which we supply oxygen (in the form of bottled oxygen) and the natural source (fumarole, fracture, volcanic plume, etc.) supplies hydrogen or other suitable fuel. The sensor derives its sensitivity and much of its selectivity from the nature of the catalytic membrane. One side of the membrane catalyzes oxidation of the fuel while the other side catalyzes oxygen reduction.

The reducing-gas sensor is shown schematically in cross section in figure 1. The sensor is housed in a solid teflon body that is resistant to fumarolic attack, and physically separates the two reactants. The perforated current collectors and conducting wires are made of gold/palladium and gold/platinum alloys to prevent corrosion. The current version of the reducing-gas sensor used in this study differs from that used in some earlier studies in that a hydrophobic teflon sheet is used to cover the fuel side of the cell providing electrical isolation of the sensor from its environment. It also prohibits water vapor penetration and particulate contamination of the electrode surfaces. A regulated gas bottle supplies oxygen to the reference side of the sensor. The rate of oxygen supply is controlled by a micrometer needle valve and is adjusted to a rate of a few liters per day.

Gas molecules diffuse through the teflon sheet and are adsorbed on the catalytic surface of the electrolyte membrane. The adsorbed molecules dissociate into ions and electrons. These

ions are then free to migrate through the membrane and react with similarly dissociated oxygen molecules. Two hydrogen ions combine with one oxygen ion to form a molecule of water. Associated with this chemical change is a corresponding electrical change that is proportional to the activity of the fuel on the catalytic surface. We measure this electrical change as a voltage drop across a load resistor connected between the two current collectors.

At 25 ^{o}C, thermodynamic data indicate that the reducing gas sensor should be able to produce a maximum of 1.23 volts output in pure hydrogen (Linden, 1984). This limitation is based on the standard potential of the reaction of hydrogen ions with oxygen to produce water. In practice however, the sensor output never gets close to this value because of losses due to electrochemical reactions, the internal resistance of the sensor, load resistance, and the relatively low concentrations of fuel used in the laboratory portion of this study or encountered in the field.

The internal resistance of the reducing-gas sensor is the sum of the electrical resistances of all of the sensor components and is an important parameter to understand because it provides opposition to the flow of electric current within the sensor. Since the load resistor is always in series with the sensor, the same current that passes through the load resistor also passes through the sensor resulting in a voltage drop equal to the product of the current and the internal resistance of the sensor. In order to measure the internal resistance of the reducing-gas sensor, we set up an experimental apparatus consisting of an impedance bridge and an external 1 kilohertz frequency source. Five reducing-gas sensors were mounted in an environmental chamber, and measurements were made over a range of temperatures from -20 to 80 ^{o}C. The results (fig. 2) indicate that the reducing-gas sensor has a low internal resistance (<10 ohms with no fuel) over the range of normal use.

The load resistance is important to the operation of the reducing-gas sensor because it helps determine the sensitivity, response time, and, to a degree, the selectivity of the sensor. When the load resistance is low (below 20k ohms), the fuel is being consumed faster, thus the sensor responds faster to changes in concentration (fig. 3). If the load resistance is sufficiently low, the sensor output will be controlled by the reactant diffusion rate and reaction kinetics thus affecting the selectivity of the sensor. Because the sensor output is measured across a resistor, low load resistances mean less voltage being dropped across the resistor, and a correspondingly lower measured output. Notice in figure 3 that at 100 ohms of load resistance, both SO_2 and H_2 produce a sensor output only slightly higher than zero. In general, a high load resistance (20K ohms and higher) corresponds to high sensitivity. The price of sensitivity is longer response time. With high load resistances, it takes longer for the sensor to reach its maximum or minimum values as the analyte gas concentration changes. For experiments discussed

herein, we used 10K ohm load resistors. This is the same value used in the field portion of the study and represents a good compromise between response time and sensitivity.

SENSOR RESPONSE CHARACTERISTICS

As stated earlier, the sensor responds to a number of gases including H_2, H_2S, SO_2, CO, COS, HCl, and HF. Our tests also indicate that the sensor does not respond to CO_2, CH_4, N_2, O_2, or He. The response of the sensor to various gases is possible to quantify, but difficult to constrain, especially for in-situ measurements. Molecules of sufficiently small size can diffuse through the protective teflon sheet. Once these molecules have diffused through the sheet, they may or may not react at the catalytic surface. Furthermore, they may dissociate on the surface of the membrane, diffuse through it, and react with the oxygen reference gas as hydrogen does, or they may react with each other on the electrode and catalytic surfaces, or they may just occupy space, diluting the effective concentrations of other gases at the surface. Gases that are both capable of diffusing through the membrane and forming hydrogen ions may elicit a sensor response. The acid gases such as H_2S, SO_2, HF, and HCl probably do just that. The reactions involving CO and COS are likely to follow some other mechanism. While CO_2 is typically present in high concentration in fumaroles and is weakly acidic, the molecular size is too great to allow it to diffuse through the teflon membrane.

To address the question of gas interferences, an experimental apparatus was designed and constructed to measure the response of five reducing-gas sensors to a single analyte gas simultaneously. With this apparatus, each of the sensors receives a programmed flowrate of reference gas (humidified oxygen) and analyte gas. The analyte gas mixture is prepared by volumetric dilution of the pure gas with ultrapure air. Once the analyte gas is introduced to the sensors, a stabilization time is required for the sensors to reach equilibrium. The typical time of an analytical run is approximately three hours, including time for the sensor to return to its normal "zero" value. The outputs of the sensors are connected to a laboratory data-acquisition system. The data are recorded and reduced in a spreadsheet database so that sensor minima (for zero analyte gas concentration) and sensor maxima (for full analyte gas concentration) can be determined.

A summary of data for 52 analytical runs at room temperature covering five gases (H_2, H_2S, SO_2, CO, and COS) is shown graphically in figure 4. The data indicate that the USGS reducing-gas sensor is more sensitive to both H_2S and SO_2 than to hydrogen. At concentrations of 25 ppm each, the sensor is about 6 times more sensitive to H_2S than to H_2, while at the 500 ppm level, the sensor is only about 1.8 times more sensitive to H_2S than to H_2. For SO_2, the sensor is 2.5 times more sensitive than

for H_2 at 25 ppm and 1.3 times more sensitive at 500 ppm. During the study we found that a group of several sensors will show the same absolute response to a given analyte gas plus or minus 25 percent. Variation of an individual sensor from one run to another with the same gas is typically smaller, generally on the order of 15 percent. The response of the sensor per unit concentration drops off as concentration increases. We interpret this drop-off to be due to inundation of the active membrane surface (a finely divided alloy of platinum and iridium black) by analyte gas. Once the active surface becomes saturated, no more analyte can reach the surface to react. This hypothesis is supported by the observation that sensitivity decreases immediately following saturation. The sensor recovers when the active membrane surface depopulates itself of analyte gas by reaction.

Sensor response to different gases over a temperature range likely to be encountered in the field was also investigated. Five reducing-gas sensors were mounted in an environmental chamber and exposed to analyte gas mixtures of H_2, H_2S, SO_2, CO, COS at five concentrations from 50 to 1000 ppm and at five different temperatures: -20, 0, 30, 60, and 80 ^{o}C. Only a single gas at a specific concentration was studied at a time over the tested temperature range. Data for each run from the five sensors were recorded at a rate of 2 data points per minute per sensor. The five sensors, each with a load resistance of 10K ohms, were allowed to stabilize for 1 hour at each temperature. The stability of the analyte gases over the temperature range was verified by gas chromatography. Sensor responses from the five sensors were averaged at each set of run conditions and the results are shown graphically in figures 5-9.

The temperature studies on sensor response produced interesting but complex results. Experiments involving SO_2 and H_2S showed the largest excursions for a given gas concentration over the temperature test range. These two gases also produced the highest response at -20 ^{o}C. It is somewhat notable that there is a signifiant response at -20 ^{o}C where internal resistance is high and ion mobility is low. The shape of the response curve for SO_2 and H_2S under conditions of high gas concentration and low temperature reflects analyte loading at the catalytic membrane surface. Simply put, SO_2 and H_2S cannot react fast enough to sustain high current through the load resistor. This is a concentration polarization effect that is especially pronounced at low temperatures with attendant slower reaction rates.

The reducing-gas sensor peaks in responsiveness to CO and H_2 at 30 ^{o}C. These two gases, along with COS, show less response variation over the temperature range of study than SO_2 and H_2S. The lower concentrations of H_2S, along with SO_2, CO, and H_2, produce a decreasing sensor response with increasing temperature, particularly at 60 ^{o}C where internal resistance of the sensor is lowest.

It is interesting to note that the overall selectivity of the reducing-gas sensor is different at higher temperatures than at room temperature. Although the sensor continues to be more sensitive to H_2S than to H_2 at 80 °C, it is slightly more sensitive to H_2 than to SO_2 at a given concentration at 80 °C (see figures 6 and 7). This reversal in selectivity between H_2 and SO_2 is also evident at 60 °C as shown in figure 3 where sensor response for different concentrations of H_2 and SO_2 is plotted against load resistance for room temperature and 60 °C. Notice also that the differences in response between H_2 and SO_2 are less at lower load resistances for both temperatures. At 80 °C, the reducing-gas sensor is more sensitive to CO than to SO_2 for gas concentrations greater than 50 ppm. The sensor is also more sensitive to CO than to H_2 at gas concentrations above 50 ppm, except at 500 ppm and above.

In summary, temperature can effect the sensor in complex ways. The sensor shows the highest response at low temperature for SO_2 and H_2S while also showing the greatest temperature effect when measuring SO_2 and H_2S. Sensor response to CO, H_2, and COS does not vary much over the temperature range studied, however, the sensor response to these three gases becomes more significant relative to SO_2 and lower concentrations of H_2S at higher temperatures. When using the sensor in the field, it should be deployed with temperature sensors whenever possible in order to better interpret the results. Indeed, it should be possible to design a reducing-gas sensor with built-in temperature compensation for field use. The temperature effects on the sensor when measuring COS are probably neglible at concentrations commonly found in fumaroles (<50 ppm, Paul Greenland, personal communication). The temperature studies on the reducing-gas sensor do not elucidate gas matrix effects, but do provide a first approximation of sensor-gas-temperature effects.

OTHER SENSOR AND INSTRUMENTATION TESTS

The temperature of gas sensor leads and sensor interface instrumentation located in the field varies by tens of degrees from day to night depending on weather conditions. The temperatures of the sensors themselves, located in fumaroles and buried in the ground, do not change very much. The only communication that a sensor has with the ground surface and the atmosphere is through its leads. Since these leads carry signal back to the interface and telemetry, and oxygen reference gas to the sensor, both temperature and pressure tests are helpful in showing that these external influences have little or no effect on sensor response. To determine the extent of any effects on sensor output due to temperature and pressure differences of sensor leads and interfacing equipment, several tests were performed with the following results:

1. Heating the load resistor did not produce a measurable change in sensor output. A reducing-gas sensor was placed in an

atmosphere of 25 ppm H_2S and allowed to stabilize at a maximum output value. The sensor leads were then heated with a heat gun from 20 °C to 55 °C for a period of 30 minutes. Following this test, the low-temperature-coefficient resistors used for sensor load resistors were heated in a similar fashion. For the 25 °C change in temperature, the sensor output showed a positive deviation of only 1 to 2.5 millivolts. The magnitude of this change is insignificant and within the noise level of the instrumentation.

2. Large barometric pressure changes should have little, if any, effect on the sensor. A reducing-gas sensor was placed in an atmosphere of 25 ppm H_2 and allowed to stabilize. The oxygen exhaust leads of the sensor were then intentionally pressurized to about 40 millibars by immersion in water. This backpressure produced a change of about -1 millivolt, which lasted 20 minutes and was followed by sensor recovery to its previous value. The magnitude of this artificially induced backpressure is more than twice the absolute value of barometric pressure change throughout the entire duration of the field portion of the experiment.

3. Temperature and supply-voltage fluctuations on sensor-interface electronics do not induce artificial changes in sensor output. The supply voltage to the interface was varied in the range of 8 to 18 volts to simulate solar panel and battery charging and discharging. No variation in the output of the sensor-interface electronics was noted. Additionally, the interface electronics were subjected to the same heat test described above. A temperature change of 25 °C produced a change of only 1 to 1.5 millivolts. Actual temperature conditions in the field do not change this much except perhaps on a yearly basis.

GAS MONITORING AT CASA DIABLO

In August 1985, the Casa Diablo portion of the Long Valley gas monitoring network consisted of three reducing-gas sensors (LVY1, LVY2, LVY3) deployed in the same small boiling-temperature fumarole in the upper clay pit area of Casa Diablo (fig. 10). One of these sensors was installed in May 1982, and the other two were installed in May 1985 along with a temperature sensor and on-site equipment for satellite telemetry. The temperature sensor was installed near the fumarole orifice only a few centimeters below ground level and is therefore subject to meteorological influence. The gas composition of fumarole LVY and two nearby fumaroles is shown in Table 1.

The upper clay pit area is located on a northwest-trending fault on the east side of the keystone graben on the resurgent dome. The orientation of the keystone graben and related faults is probably controlled by the general northwest trend of regional structures along the eastern front of the Sierra Nevada (Bailey et al, 1976). The upper clay pit area is extensively hydrothermally altered to clay, dominantly kaolinite (Rinehart and Ross, 1964), and is one of several small areas of

argillaceous alteration aligned along the eastern keystone graben fault. These areas presumably formed as a result of hydrothermal alteration owing to fumarolic and hot-spring activity. Weak fumarolic activity still exists today in most of these areas.

During August and September 1985, we deployed ten additional reducing-gas sensors at four stations on or near the eastern keystone graben fault (fig. 10). Station CDX was established about 25 m south of station LVY. Sensor CDX1 was installed in a small boiling-temperature fumarole in the middle of the altered area and presumably in the middle of the fault zone. Sensor CDX2 was installed in warm ground at the eastern edge of the altered area. Sensor CDX3 was buried in soil several meters to the east completely out of the altered area and fault zone.

Station CDY was established about 25 m north of station LVY. Sensor CDY1 was installed in a 1-m-deep pit dug into hot clay in the center of the altered area. Sensor CDY2 was buried in warm ground at the eastern edge of the altered area. CDY3 was installed in a 1-m-deep pit in soil about 50 m west of the fault zone. Another gas sensor, CDW7, was buried 1 meter deep in soil about 75 m east of the fault zone at the site of the weather station.

The fourth reducing-gas monitoring station, Casa Diablo North (CDN), was established 400 m north of station LVY on the eastern keystone graben fault. CDN is in an area of recent tree kill first noticed in 1982, although no alteration or fumarolic activity is visible at the surface in the immediate area. The ground is warm (40-60 ^{o}C) at 1-m depth. Sensor CDN1 is at the presumed eastern edge of the eastern keystone graben fault near the base of a bluff. Sensor CDN2 is midway down the hill about 10 m west of CDN1. CDN3 is 10 m west of CDN2 near an abandoned road. All three sensors were buried 1 m in the warm soil. Soil temperatures are progressively warmer from CDN1 to CDN3. A small area of surface alteration, with a maximum temperature of 81 ^{o}C, is present several meters northeast of station CDN.

Data for the 13 gas sensors (3 existing and 10 new) and 1 temperature sensor during August and September 1985 are shown in figures 11-15. Except for weak intermittent diurnal variations, data from the three sensors some distance away from the altered areas and off the fault structure (CDX3, CDY3, and CDW7) show no significant variation after a short settling-in period. Data from two sensors installed at the eastern edge of the lower clay pit (CDX2 and CDY2), as well as data from CDN3, are equally uneventful. Data from the remaining seven sensors (LVY1, LVY2, LVY3, CDX1, CDY1, CDN1, AND CDN2), however, show significant variations, both diurnal and systematic (i.e. responsive to the system); these variations are discussed later in the report.

METEOROLOGICAL DATA

Meteorologic measurements were made to test the effect of weather on the sensors. On August 10, 1985, a solar-powered weather station (CDW) was installed on the resurgent dome near Casa Diablo about 75 m southeast of station LVY (fig. 10). The station consisted of sensors for wind direction, wind speed, air temperature, relative humidity, barometric pressure, and rainfall. The interface electronics for the rainfall sensor (tipping bucket rain gauge) did not function properly, so precipitation data reported here are taken from daily measurements made by the U.S. Forest Service at the Mammoth Ranger Station 5 km to the west. Total precipitation was collected every 24 hr in an 8-inch standard U.S. Weather Bureau rain gauge. Data for the meteorologic parameters measured during August and September 1985 are shown in figures 16 and 17.

All of the parameters, except rainfall, show diurnal variations. Air temperature begins to increase about 1600 GMT (8:00 a.m. local standard time) and reaches a maximum about 2200 GMT (2:00 p.m.). Air temperature reaches a minimum daily value about 1400 GMT (6:00 a.m.). The daily variation in temperature for the period of record was typically 15 to 20 ^{o}C.

Daily variations in barometric pressure occur, but the changes over several days far exceed these daily variations. The maximum daily barometric pressure occurs around 1600 GMT (8:00 a.m.) and the minimum is in the late afternoon at about 0100 GMT (5:00 p.m.). The magnitude of daily changes in barometric pressure is typically only 1 or 2 millibars, and the change in barometric pressure for the entire period is about 16 millibars.

The diurnal maxima and minima for relative humidity cover a wide range and vary significantly, with minimum values between 1800 GMT (10:00 a.m.) and 2400 GMT (4:00 p.m.) and maximum values between 0400 GMT (8:00 p.m.) and 1600 GMT (8:00 a.m.). Relative humidity values between 5 percent and 92 percent were measured during August and September.

The dominant winds for the region are out of the west-southwest. At about 0700 GMT (11:00 p.m.), the wind direction typically shifts abruptly from this direction to the northeast. Sharp reversals often occur at night, but the winds generally remain out of the northeast until about 1600 GMT (8:00 a.m.), when they reverse again and begin blowing from the southwest. During daylight hours the wind direction typically shifts slightly from the southwest to the west-southwest. Wind speed usually begins to increase about 1600 GMT (8:00 a.m.) and reaches a maximum within an hour or two, and remains there until about 0400 GMT (8:00 p.m.), when it drops off for the night. Maximum wind speeds during August and September were typically around 8 mph and minimum wind speeds at night were usually about 1 or 2 mph.

At least three significant perturbations in the meteorologic data during August and September are associated with recorded precipitation. The first episode occurred on September 3-4. Rainfall amounts of 0.31 in. and 0.32 in. were measured on September 3 and 4 respectively. According to U.S. Forest Service records, this was the first recorded rainfall in the region since July 26.

The second episode occurred on September 11, when 0.99 inches of precipitation, mostly snow, were measured. The snowfall began about 0300 GMT and lasted for several hours. Accumulations from 6 in. to 8 in. were observed in the town of Mammoth Lakes, and accumulations of 4 in. to 6 in. were noted late on September 11 in the Casa Diablo area. Lightning accompanied the snowfall from 0500 to 0800 GMT on September 11.

The third episode of precipitation occurred on September 18, when 0.19 in. of rain fell. This was the smallest and most localized of the three precipitation events. Probably little or no precipitation fell in the Casa Diablo area, 5 km east of the rain gauge.

All three episodes were accompanied by decreased barometric pressure and air temperature and increased relative humidity. The episode of September 3-4 was accompanied by distinctly decreased wind speed.

Another significant meteorologic event, not related to the three episodes of precipitation, was an increase in relative humidity and a decrease in air temperature on August 17-18. These events followed a barometric-pressure minimum, which began on August 16, and can be explained by adiabatic expansion of air subjected to lowered pressure, which results in cooling. Since relative humidity is a measure of the amount of water vapor a given quantity of air can hold at a given temperature and pressure, it follows that relative humidity will increase when air temperature falls, because the air's capacity for moisture is lowered. This phenomenon can be easily seen in figures 18 and 19, where the diurnal maxima for relative humidity and air temperature are 180^{o} out of phase.

DIURNAL VARIATIONS AND METEOROLOGIC FACTORS

Solar radiation is the ultimate source of energy for the earth's atmosphere, so it is plausible that the radiant energy received from the sun (insolation) plays a dominant role in most, if not all, diurnal processes at the earth's surface. Fluctuations in the amount of insolation reaching the earth's surface, as well as variations in the nature of the earth's surface, often cause uneven heating of the earth's lower atmosphere (Donn, 1965). Heat provides the energy for all atmospheric processes, so that irregular heating must greatly affect many near-surface processes. Monitoring meteorologic

parameters that reflect uneven heating, and assessing local conditions enable evaluation of the effect of insolation on the microclimates in the Casa Diablo area.

Although not well developed, the idea that solar insolation plays an important role in causing diurnal variations in soil degassing was suggested by Sato et al (1986). Earlier, Sato and McGee (1981) postulated that orographic winds were the cause of diurnal variations in degassing at Mount St. Helens measured by reducing gas sensors on the flanks of the volcano.

We observed a diurnal pattern of degassing at one time or another at virtually every site instrumented with a reducing-gas sensor. At some sites variations are consistent and regular, while at other sites variations disappear or become intermittent. Understanding the cause of diurnal variations is important to understanding the process of degassing, because gas events recorded in the past, particularly at Casa Diablo during 1983 and 1984 (our unpublished data), have often coincided with the diurnal maximum. Likewise, large amplitude negative spikes have sometimes occurred near the diurnal minimum. Factors, meteorologic or otherwise, that cause such apparent diurnal variation in degassing need to be understood, so that truly anomalous degassing behavior can be readily identified and interpreted.

The times of diurnal maxima and minima recorded by the reducing-gas sensors are typically very consistent for each monitoring station but can vary considerably between sites. For the sites in the Casa Diablo area, all within a few hundred meters of one another, the diurnal minima generally occur during daylight hours, from morning through mid-afternoon, whereas the diurnal maxima begin in late afternoon to early evening and typically persist through the hours of darkness. The diurnal minima are usually, but not always, of shorter duration than the maxima.

If the meteorologic data during periods of no rainfall are compared with data from selected reducing-gas sensors, it becomes evident that there is an interrelationship. Shown in figures 18, 19, and 20 are data from three gas sensors (CDX1, CDN1, and LVY1) plotted with meteorological data for a 5-day period beginning on September 18. The plot labeled BATTERY-SOLAR (fig. 20) is actually a plot of battery voltage at monitoring station CDX. Since a solar panel is used to charge the station batteries, this plot can be considered proportional to the amount of solar radiation reaching the earth's surface in the Casa Diablo area. Note especially the last three days of the time period. Diurnal patterns are well developed for the gas sensors and all of the meteorological parameters except for barometric pressure. Note also that diurnal minima for the gas sensors all occur during daylight hours ranging from CDX1 in the early morning, to CDN1 in the afternoon. This is also the time of westerly winds and when solar radiation, air temperature, wind speed are either at

maximum or beginning to rise. Likewise, the times for the beginning of diurnal maxima for the reducing-gas sensors range from late afternoon (CDX1) to after midnight local time (CDN1).

A partial explanation for this is evident upon close examination of the wind direction data. As discussed earlier, the dominant daytime winds for the area of study are out of the west-southwest. During evening hours wind direction typically shifts abruptly to the northeast.

Inspection of topographic features of the area (fig. 10) reveals that daytime winds travel upslope while winds during the night travel downslope. This is the widely known phenomenon of orographic winds, often called mountain and valley winds, and is a process by which solar heating and radiational cooling influence local winds in mountainous settings (Stern et al, 1984). During the daytime, solar heating, or insolation, warms the slopes. As the density of the air adjacent to the slope decreases, the air moves up the slope resulting in a valley wind. On clear nights, the higher slopes radiate heat causing the land and adjacent air to be cooled. This cool dense air mass then begins to flow downslope resulting in a mountain wind. Intuitively, it would be expected that this downward flow of dense air would create higher pressure at the ground surface and inhibit degassing, in a relative sense, while the converse would be true for winds traveling upslope.

Data from reducing-gas sensors at Casa Diablo generally suggest just the opposite since diurnal maxima occur at night and minima occur in the daytime. One plausible explanation for this is that when degassing to the surface is inhibited by higher pressure or the presence of a layer of cool dense air, the population of gaseous molecules for the sensors, located underground, actually increases. Likewise, increased degassing to the surface may result in a lower density of gas molecules in the near subsurface. In other words, in a setting where there is a low constant gas flux from depth to the surface, a decrease in degassing to the surface caused by meteorologic or other atmospheric factors may actually result in an apparent increase in gas concentration as measured by sensors located a short distance below ground level.

Although other factors not described here may prove to be of equal or greater importance, it is likely that the microclimates near each of the sensors also play an important role in controlling or modifying degassing patterns. Air motion can be strongly influenced by the friction of the earth's surface and by thermal convection if the surface is warmer than the overlying air (Geiger, 1965). Since the area near the monitoring sites is dotted with fumaroles, boiling mud pots, and patches of warm ground, it is easy to imagine local convection cells centered over the sources of heat. Since low pressure is associated with the bottom of an ascending air mass, the existence of these convection cells could tend to stabilize degassing rates.

As discussed earlier, wind speed drops off typically to 1-2 miles per hour during the night. The condition of very light downslope winds at night along with lower air temperatures probably favors the formation of convection cells. If the convection cells remain relatively undisturbed by winds or precipitation, a steady-state degassing condition could be expected during nighttime hours. However, during daytime, wind speeds range from 5 to 9 miles per hour. These faster upslope winds probably enhance subsurface-surface gas exchange resulting in apparent depletion of gas at shallow depths where the sensors are located. In addition, increased air flow will cause an increase in turbulence in proportion to the roughness (friction) of the terrain. Eddies would then form which can produce local wind gusts and lulls. This may explain the often erratic baseline degassing behavior recorded by sensors LVY1, LVY2, LVY3, and CDX1, the only sensors installed in fumaroles. The LVY fumarole is several meters deep and has an orifice about 15 cm in diameter partially covered with rocks. The sensors are installed at a depth of about 3 meters. Because this fumarole has very low flow, the apparent degassing recorded by the gas sensors could be influenced by strong wind gusts and lulls at the surface. The fumarole in which sensor CDX1 is installed is smaller than LVY and located at the base of a small slope. Its orifice is similar in size to that of LVY but sensor CDX1 was only inserted to a depth of about 0.3 m. Since the sensor is located at a rather shallow depth, degassing patterns recorded by the sensor could presumably be influenced to a large extent by wind gusts and lulls and other factors related to the microclimate in the immediate area. If we assume that the degassing rate over the time period of this study was constant (i.e. no anomalous contribution of gas from depth), then it is probable that apparent increases and decreases from this baseline are created by complex competing forces that differ in the magnitude of their influence at each site.

During the course of this study, we observed that diurnal degassing changes are more pronounced during periods of clear weather. Although the soil in the Casa Diablo area may not have exactly the same pore space, a typical silt loam soil contains about 50 per cent pore space divided roughly in half between water and air depending on rainfall and local soil conditions (Buckman and Brady, 1969). The diffusion of gases from the soil to the atmosphere is controlled by the partial pressure of each gas in the soil relative to that in the atmosphere. Since the pressure of a gas is temperature-dependent (with constant volume), the soil temperature will influence the tendency of soil gases to escape to the atmosphere. The amount of heat absorbed by soils is a direct function of the amount of solar radiation reaching the earth as modified by certain other factors such as the color of the soil, the amount of vegetative cover, and the slope of the soil surface with respect to the angle of incidence of the sun. Much of the solar radiation reaching the earth is, in turn, re-radiated back into space, particularly during periods of clear weather. Because the presence of cloud cover limits the

effectiveness of solar radiation in heating and cooling the earth, it can be expected that the daily change in soil temperature will be greater during periods of clear weather.

Although the soil gas sensors in this experiment were installed at depths generally considered to be near the limit of influence of daily temperature changes, the effects of depletion or enhancement of gases near the soil surface probably extend to greater depths due to diffusion of gases within the soil. For example, sensor CDW7 was buried 1 meter deep in soil at the site of the weather station. A plot of CDW7 for the period of the experiment shows that small diurnal changes in reducing-gas emission are present during the first half of the period but generally disappear in early September for about 3 weeks then reappear again during the last few days of the experiment (fig. 15). Examination of rainfall data for the period of the experiment (fig. 16) shows that all of the recorded rainfall occurred during the same period when gas diurnals were absent at CDW7. Since cloudy weather would typically accompany rain, these data corroborate the idea that the presence or absence of cloudy weather can influence diurnal degassing patterns.

Supporting evidence for the contention that insolation is an important controlling influence on diurnal degassing patterns can be seen by again examining the data for September 18-19 in figures 18, 19 and 20. The subdued solar radiation peak on September 18 shown on the battery voltage plot in figure 20 indicates a cloudy day. A cloudy period means that there will be less radiational cooling at night resulting in less driving energy for orographic winds. Indeed, inspection of the wind direction plot on figure 20 reveals no orographic winds on September 18 and only a 2-hour period of orographic winds on September 19. The wind-speed data on figure 13 supports this by revealing that winds on the night of September 18 were about 3-4 miles per hour (i.e. somewhere between normal daytime and nighttime conditions). If that is the case, then the convection cells in the Casa Diablo area were probably disturbed during the night much as they usually are during the daytime. The higher wind speeds would result in aspiration of gases from fumaroles and near-surface soils thereby creating conditions similar to those during daylight hours. Indeed, inspection of the data from CDX1, CDN1, and LVY1 on figure 20 reveals an absence of normal nighttime diurnal maxima during that period.

Since air is a compressible gas, the barometric pressure of air is a function of its density as modified by regional and global factors. Density, in turn, is a function of temperature and the amount of water vapor in the air. Daily variations in regional barometric pressure are very small when compared with variations over several days. Although apparent diurnal degassing patterns vary in sympathy with barometric pressure, their minima and maxima do not exactly correspond. In addition, degassing does not seem to vary significantly with many of the larger long-term changes in barometric pressure. We suspect,

therefore, that local pressure variations caused by wind effects on the microclimate at the surface of the ground exert more influence over the timing of degassing than regional changes in barometric pressure.

CORRELATION OF REDUCING GAS EVENTS WITH RAINFALL

The most striking reducing-gas events for the period of record occur during the first half of September. Excursions from the normal baseline can easily been seen on the plots for LVY1-3 and CDX1, and to a lesser degree on CDY1 and CDN2. These data, along with vertical bars representing rainfall, are shown in figures 21-25. There is clear relationship between the two data sets. Following the rainfall on September 3, there are sharp negative spikes in the data for LVY1 and LVY3 and a sharp positive spike in the data for LVY2 followed by a second positive spike of longer duration. The same pattern occurs in conjunction with the snowfall of September 11 except that all of the initial excursions are negative for the LVY gas sensors. In addition, sensor CDX1 also shows a negative deflection around the same time, although a gap in the data prevents determination of the exact time.

As discussed earlier, sensors LVY1, LVY2, LVY3, and CDX1 are the only sensors installed in fumaroles. As a result, they probably have better communication with the hydrothermal system than the other sensors. It seems feasible to us that the addition of cold water (particularly snowmelt on September 11) to the upper part of the hydrothermal system could temporarily quench these fumaroles causing a decrease in the gas vapor pressure. This is supported by a recorded temperature decrease at LVY on September 11 (fig. 11) and would explain decreases in apparent gas concentration reaching the sensors. Another explanation could be that the sensors themselves are influenced by temperature, and, indeed, our laboratory tests indicate that the sensor is more sensitive to H_2S and SO_2 at lower temperatures. The positive peaks recorded by sensor LVY2 following the first precipitation event are anomalous and we cannot explain them at this time.

Sensor CDY1, installed in hot clay in the center of the fault zone, seems to have responded to a small degree to the second, and larger, precipitation event in concert with sensor CDX1 and the three LVY sensors. The sensors in the warm ground at Casa Diablo North did not respond with the timing or to the degree that the LVY sensors did. Sensor CDN2 did have a small positive excursion a couple of days after the first rain. This was followed by a slow decrease and an even slower climb back toward the earlier baseline. Sensor CDN1 recorded a one-day diurnal maximum during this time period. Whether or not this is related to precipitation is subject to speculation. Sensor CDN3 did not record any significant change during the periods of precipitation. The different behavior of the CDN sensors from

the sensors described earlier might be due to the higher elevation at CDN or to complex subsurface circulation patterns.

The sensors known to be either directly adjacent to the altered areas or some distance away (CDX2, CDX3, CDY2, CDY3, and CDW7) did not record any significant changes during or after any of the precipitation events. This is not surprising since the sensors used in this experiment, unlike earlier versions used in other studies, are sealed with a teflon sheet to prevent entry or exit of moisture. Only gaseous molecules of sufficiently small size can enter the interior of the sensor. In fact, plunging the current version of the sensor into water produces a neglible effect on the sensor output. In other words, we know of no inherent reason in the design or construction of the current version of the sensor that would produce any response to rainfall or moisture. Reimer (1980) suggested that significant amounts of rainfall could saturate upper soil layers and thereby inhibit the normal release of soil gas to the atmosphere creating a temporary zone of increased gas concentration in the near-surface soil layers. This idea seems very plausible to us but we can find no strong evidence in support of it in our Casa Diablo data. It may be that this process, if valid, would be less effective for light gases such as hydrogen than for heavier gases.

CORRELATION OF REDUCING GAS EVENTS WITH CASA DIABLO SEISMICITY

In order to determine whether a relationship exists between degassing and hydrothermal-system microseismicity, a Mark Products, Inc. L-4 seismometer (frequency 2 hz) was installed on solid rock at the bottom of a 1-m-deep hole about 75 m northeast of station LVY on August 9, 1985. Seismic data were recorded onsite on a battery-powered Teledyne Geotech Portacorder. Instrument gain was typically set to 60 dB, and the recorded data were retrieved every two days. Nearly 200 earthquakes were recorded at Casa Diablo during August and September.

These earthquakes were compared with USGS computer files. Earthquakes with locations outside of the Casa Diablo area were eliminated from the list. The remaining earthquakes were examined for S-P interval. Those with anything but a very short S-P interval were also eliminated from the list, leaving only those earthquakes local to the Casa Diablo area. These earthquakes typically had coda magnitudes of 0.5 or less and are thought to be associated with the hydrothermal system.

The Casa Diablo earthquakes are shown as vertical lines in figure 26 along with vertical bars representing precipitation. The two periods of most frequent earthquake activity appear to be associated with the two larger precipitation events and are probably due to percolation of water into the top of the hydrothermal system. The few other earthquakes not obviously associated with precipitation appear to have occurred at random. Unfortunately, other than the rainfall-induced

seismicity, no other significant seismic events seem to have occurred, and the current seismic network in Long Valley does not seem to have the resolution to detect microseismicity in the hydrothermal system on a regular basis. As a result, it is inconclusive whether a relationship between degassing and hydrothermal system seismicity exists or not.

CORRELATION OF REDUCING GAS EVENTS WITH CALDERA SEISMICITY

Our data indicate that local ground motion caused by earthquakes within the caldera does not cause degassing events. Records of earthquakes occurring within Long Valley caldera were obtained from computer files kept by the USGS. Plots of gas sensor data with caldera earthquakes shown as vertical lines, with length proportional to magnitude,at the bottom are shown in figures 27-31. No unusual seismicity occurred during the experiment. Caldera earthquakes occurred at random times throughout August and September and there appears to be no correlation with the degassing data.

THE INFLUENCE OF EARTH TIDES ON DEGASSING

We do not see a correlation between earth tides and diurnal degassing. Earth tides are generated primarily from the gravitational attraction between the earth, sun, and moon. As the movements of the sun and moon with respect to the earth can be accurately predicted, and the axis and period of rotation of the earth are well known, tidal forces can be easily calculated (Longman, 1959, Pollack, 1973). The earth's rotation every 24 hours causes the largest tidal fluctuations and generates both semidiurnal and diurnal tidal components. The amplitudes of these daily tides are then modulated by longer period tidal forces to intermittently produce both higher- and lower-than-normal tidal forces.

Shown in figures 32-36 are plots of earth tidal forces superimposed on plots of gas data for each of the monitoring locations. Diurnal variations in degassing occur at the same time each day, while the timing of tidal forces varies from day to day. In addition, degassing minima and maxima occur at different times of day for different monitoring sites. It is conceivable, however, that under the right circumstances, earth tidal forces could trigger certain gas related events. Presumably, dilation of fractures and pores in the earth can occur with strong tidal forces while compression might occur with weak tidal forces. Rinehart (1980) reports that tidal forces have been observed to affect geyser activity; however, no such correlation can be established for degassing at Casa Diablo based on available data.

ANALYSIS OF FUMAROLE GAS BY GAS CHROMATOGRAPHY

One of the field tasks was to check the performance of USGS reducing-gas sensors located in fumaroles by an independent method such as gas chromatography. Since we wanted to determine whether the diurnal pattern typically recorded by our sensors was a real change in degassing or simply caused by meteorological or other influences on the sensor, we set up an experiment to sample and analyze light gases by gas chromatography from fumarole LVY every 3-4 hours for a 24-hour period.

During reconnaissance in Long Valley in 1985, we determined that hydrogen concentrations in both fumarole and soil-gas samples from the Casa Diablo area ranged from 0.5 to 100 ppm. Because most commercially available gas chromatographs are not capable of quantifying hydrogen at such low concentrations, a simple analytical instrument with high sensitivity for light gases, as well as the added features of high sample throughput and transportability, was developed for use in this experiment (Sutton, 1987). This instrument is an ambient-oven gas chromatograph with a multifunctional ten-port valve and a micro-volume thermal-conductivity detector.

The design of the gas chromatograph allows both flow-through bottle and syringe samples to be reproducibly introduced into the instrument. Light gases such as hydrogen, helium, and neon can be separated as a group from unwanted gases (O_2, N_2, CO_2, H_2O, etc.) on a precolumn. Unwanted heavy gases, which can degrade the performance of the column and detector, are backflushed to a vent while gases of interest are separated from each other on an analytical column under an argon carrier gas. The use of backflushing also cuts the time for an analysis by one-half. The output from the instrument is connected to a recording integrator which records the chromatogram and integrates the peak areas. The sensitivity of the instrument is at the low ppm level for the gases of interest.

A 1.25 cm O.D. CPVC tube, perforated along the bottom end, was inserted into the LVY fumarole to facilitate sampling. Gas samples were drawn out through the tube into glass flow-through sampling bottles by a small hand pump and analyzed for hydrogen by the instrument described above. The results of this 24-hour sampling and analysis experiment for LVY and two nearby fumaroles (MCF and LCD) are shown in figure 37.

The data from this experiment support the conclusion that gas flux varies during a day, but the timing of the minima and maxima seem differ from those measured by the reducing-gas sensors. An apparent minimum in the 24-hour data occurs during the early evening hours while the gas-sensor values are increasing or already at maximum. There is a hint of an intriguing relationship with orographic winds shown in figure 38 where wind direction data are superimposed on the 24-hour data. Notice that for two of the three fumaroles, a minimum value for

hydrogen occurs after the shift of winds from upslope to downslope. Likewise, a maximum in hydrogen concentration for all three fumaroles seems to occur just after the shift back to upslope winds in the morning. The timing of these events may just be an accident related to the time the samples were taken. The 24-hour data consist of only eight values of hydrogen concentration while the gas-sensor data are recorded on a 10-minute interval and reflect the concentration of a gas mixture, since hydrogen sulfide is known to be present in LVY fumarole albeit in low concentrations. Since the results of the present study indicate that the USGS reducing gas sensor is more sensitive to hydrogen sulfide than to hydrogen at low concentrations, the heavier H_2S is likely the dominant contributor to the data produced by the reducing-gas sensors.

STRUCTURAL CONTROL OF DEGASSING

In order to determine the influence of geologic structure on degassing, we made several soil-gas surveys of hydrogen flux across the Casa Diablo area. For each soil-gas sample, a 1.25 cm O.D. CPVC tube, perforated at the bottom, was driven into the ground to a depth of 0.6 m and capped with a rubber septum. Approximately 24 hours later, a sample of the headspace gas was withdrawn from the tube by syringe and analyzed by the gas chromatograph described in this report. Along with hydrogen, neon gas was readily detectable in nearly all of the samples. Assuming that there is no reason for neon to vary in soil gas with respect to atmospheric hydrogen, all of the hydrogen values were normalized to neon by calculating the H2/Ne ratio. This was done to eliminate any variation in the results that might be due to instrument baseline drift or changes in instrument sensitivity. The results from one of the soil gas traverses, shown as line B-B′ on figure 10, are plotted in figure 39 and reveal a large spike in the H2/Ne ratio coincident with the trace of the eastern keystone graben fault. Equally dramatic are the minima on either side of the peak. These results agree with earlier described results of the array of reducing-gas sensors deployed on and off the fault and suggest that geologic structure plays a very important role in controlling degassing patterns at the earth's surface.

CONCLUSIONS

The design of the USGS reducing-gas sensor is based on that of a fuel cell. This electrochemical sensor is simple in design yet complex in performance. Unlike most commercially-available chemical sensors, it will withstand direct insertion into fumaroles or steam vents up to temperatures of 100 ^{o}C or more. It is impervious to highly corrosive acid gases and operates without need of external electrical power. Although temperature and load resistance affect its sensitivity and selectivity, it measures a variety of gases including hydrogen sulfide, sulfur

dioxide, hydrogen, carbon monoxide, carbonyl sulfide, hydrogen chloride, and hydrogen fluoride. It is not sensitive to carbon dioxide, methane, nitrogen, oxygen, or helium.

Several reducing-gas sensors were deployed in Long Valley caldera for 2 months in 1985 along with instrumentation to record seismicity and various meteorological parameters. Data from the reducing-gas sensors show a well developed diurnal pattern. Gas samples taken from three fumaroles over a 24-hour period and analyzed by gas chromatography show that natural degassing also varies during a day. Comparison of gas-sensor data with meteorological data indicates a strong relationship between diurnal degassing from both fumaroles and the soil and orographic winds. This suggests that solar insolation (i.e solar heating and radiational cooling) may exert an important influence on degassing from natural sources. It is also likely that local microclimates influence degassing to a varying degree. No relationship between barometric pressure or earth tides and degassing was detected. Data from the reducing-gas sensors installed in low-temperature fumaroles with weak flow show distinct changes apparently related to the occurrance of precipitation events. Since moisture does not directly affect the reducing-gas sensor, rainfall may be quenching the upper portion of the hydrothermal system thereby affecting gas output through the fumaroles.

Comparison of gas data and seismic data indicates that local ground motion caused by earthquakes within Long Valley caldera does not produce measurable degassing events. However, results from an array of reducing-gas sensors deployed both on and off a fault as well as data from a soil gas sampling traverse across a fault suggest that geologic structure may play an important role in influencing the location and extent of degassing.

LIST OF REFERENCES

Bailey, R. A., Dalrymple, G. B., and Lanphere, M. A., 1976, Volcanism, structure, and geochronology of Long Valley Caldera, Mono County, California: Journal of Geophysical Research, v. 81, no. 5, p. 725-744.

Buckman, H. O., and Brady, N. C., 1969, The nature and properties of soils (7th ed.): New York, The Macmillan Company, 653 p.

Critchfield, H. J., 1966, General climatology (2nd ed.): Englewood Cliffs, New Jersey, Prentice-Hall, Inc., 420 p.

Donn, W. L., 1965, Meteorology: New York, McGraw-Hill, 484 p.

Geiger, Rudolf, 1965, The climate near the ground: Cambridge, Massachusetts, Harvard University Press, 611 p.

Giggenbach, W. F., 1975, A simple method for the collection and analysis of volcanic gas samples: Bulletin Volcanologique, v. 39, n. 1, p. 132-145.

Linden, D. I., 1984, Handbook of batteries and fuel cells: New York, McGraw-Hill, Inc., 1088 p.

Longman, I. M., 1959, Formulas for computing the tidal accelerations due to the moon and the sun: Journal of Geophysical Research, v. 64, p. 2351-2355.

Malone, S. D. and Frank, David, 1975, Increased heat emission from Mount Baker, Washington: Transactions, American Geophysical Union, v. 56, p. 679-685.

McGee, K. A., Casadevall, T. J., Sato, M., Sutton, A. J., and Clark, M. D., 1982, Hydrogen gas monitoring at Long Valley Caldera, California: U.S. Geological Survey Open-File Report 82-930, 12 p.

Pollack, H. N., 1973, Longman tidal formulas: resolution of horizontal components: Journal of Geophysical Research, v. 78, p. 2598-2600.

Reimer, G. M., 1980, Use of soil-gas helium concentrations for earthquake prediction: limitations imposed by diurnal variation: Journal of Geophysical Research, v. 85, n. B6, p. 3107-3114.

Rinehart, C. D. and Ross, D. C., 1964, Geology and mineral deposits of the Mount Morrison quadrangle, Sierra Nevada, California: U. S. Geological Survey Professional Paper 385, 106 p.

Rinehart, J. S., 1980, Geysers and geothermal energy: New York, Springer-Verlag, 223 p.

Sato, M., Malone, S. D., Moxham, R. M., and McLane, J. E., 1976, Monitoring of fumarolic gas at Sherman Crater, Mount Baker, Washington: Transactions, American Geophysical Union, v. 57, p. 88-89.

Sato, M. and McGee, K. A., 1981, Continuous monitoring of hydrogen on the south flank of Mount St. Helens: in Lipman, P. W. and Mullineaux, D. R., eds., The 1980 eruptions of Mount St. Helens volcano, Washington: U. S. Geological Survey Professional Paper 1250, p. 209-219.

Sato, M., Sutton, A. J., McGee, K. A., and Russell-Robinson, S., 1986, Monitoring of hydrogen along the San Andreas and Calaveras Faults in Central California in 1980-1984: Journal of Geophysical Research, v. 91, n. B12, p. 12,315-12,326.

Stern, A. C., Boubel, R. W., Turner, D. B., and Fox, D. L., 1984, Fundamentals of air pollution (2nd ed.): Orlando, Florida, Academic Press, Inc., 530 p.

Sutton, A. J., 1987, A chromatographic system for the analysis of selected light gases in geothermal and volcanic systems: U. S. Geological Survey Open-File Report 87-13, 13 p.

Table 1. Analyses of dry gas (in mole percent) from fumaroles in the Casa Diablo area, Long Valley, California. All samples were taken on September 29, 1985 using evacuated sampling vessels containing alkaline solutions (Giggenbach, 1975). Samples were collected by the authors and analyzed at the U. S. Geological Survey in Menlo Park, CA (C. Janik). BDL indicates that the concentration of the gas was below the detection limit of the analytical instrumentation. The sampling locations are shown on figure 10.

Fumarole & T °C	CO_2	H_2S	H_2	CH_4	NH_3	N_2	Ar	O_2	He (ppm)
LVY[1] 93°	16.35	0.093	BDL	BDL	0.076	64.1	0.76	17.2	BDL
MCF[2] 93°	94.90	1.074	0.12	0.13	BDL	3.5	0.07	0.04	7.7
LCD[3] 96°	94.73	0.876	0.097	0.11	0.261	3.8	0.08	0.02	21.7

[1]Fumarole LVY is the location of three reducing gas sensors (LVY1, LVY2, & LVY3). It has weak flow and is dominantly air.

[2]Fumarole MCF is a small fumarole in the altered zone near Mud Crater.

[3]Fumarole LCD is the largest fumarole in the clay pit area. It has vigorous flow and has been sampled by several investigators in the past. It is often referred to as CDF fumarole.

FIGURE CAPTIONS

FIGURE 1. Schematic diagram of the USGS reducing-gas sensor showing both top and side views in cross section.

FIGURE 2. Two plots showing the internal resistance of the USGS reducing-gas sensor as a function of temperature. Measurements for the top plot were made under ambient atmospheric conditions while those for the bottom plot were made in an atmosphere of 500 ppm hydrogen. Internal resistance measurements were made using an impedance bridge and an external frequency source. Since alternating current with a frequency of 1 kilohertz was used for the measurements instead of direct current, the measured parameter is more accurately termed internal impedance. Because the alternating current was of such high frequency (1 kHz) and since the reactions at the catalytic membrane are reversible, no net chemical reaction occurs under such conditions. Therefore, the measured impedance is essentially the same as internal resistance.

FIGURE 3. The top plot shows measured values of reducing-gas-sensor output in millivolts for load resistance values from 100 ohms to 100K ohms for 50 ppm H_2 and 50 ppm SO_2. The bottom plot is similar except that the measurements were made in an environmental chamber at 60 ^{o}C for 500 ppm H_2 and 500 ppm SO_2.

FIGURE 4. Plot showing USGS reducing-gas-sensor response to a range of concentrations of H_2S, SO_2, H_2, CO, and COS at room temperature. The vertical axis for this and all other figures showing sensor response is the output of the sensor measured in millivolts (mv).

FIGURE 5. Plot showing USGS reducing-gas-sensor response to five different concentrations of hydrogen sulfide from 50 to 1000 ppm at five temperatures from -20 to 80 ^{o}C. Each run started with the sensors in an environmental chamber at -20 ^{o}C. The onset of the steep rise in the response curves represents the arrival of analyte gas at the sensors. The sensors were allowed to stabilize for 1 hour before the environmental-chamber temperature was increased to the next value.

FIGURE 6. Plot showing USGS reducing-gas-sensor response to five different concentrations of sulfur dioxide from 50 to 1000 ppm at five temperatures from -20 to 80 ^{o}C. Each run started with the sensors in an environmental chamber at -20 ^{o}C. The onset of the steep rise in the response curves represents the arrival of analyte gas at the sensors. The sensors were allowed to stabilize for 1 hour before the environmental-chamber temperature was increased to the next value.

FIGURE 7. Plot showing USGS reducing-gas-sensor response to five different concentrations of hydrogen from 50 to 1000 ppm at five temperatures from -20 to 80 °C. Each run started with the sensors in an environmental chamber at -20 °C. The onset of the rise in the response curves represents the arrival of analyte gas at the sensors. The sensors were allowed to stabilize for 1 hour before the environmental-chamber temperature was increased to the next value.

FIGURE 8. Plot showing USGS reducing-gas-sensor response to five different concentrations of carbon monoxide from 50 to 1000 ppm at five temperatures from -20 to 80 °C. Each run started with the sensors in an environmental chamber at -20 °C. The onset of the rise in the response curves represents the arrival of analyte gas at the sensors. The sensors were allowed to stabilize for 1 hour before the environmental-chamber temperature was increased to the next value.

FIGURE 9. Plot showing USGS reducing-gas-sensor response to four different concentrations of carbonyl sulfide from 50 to 1000 ppm at five temperatures from -20 to 80 °C. Each run was started with the sensors in an environmental chamber at -20 °C. The sensors were allowed to stabilize for 1 hour at each temperature. The 250 ppm curve is anomalous and we can not explain it.

FIGURE 10. Map of the Casa Diablo area of Long Valley caldera, California showing the eastern keystone graben fault, fumaroles, reducing gas monitoring sites, and location of the soil-gas sampling traverse.

FIGURE 11. Data for the period August 12 to September 27, 1985 from three reducing-gas sensors and one temperature sensor at monitoring site LVY. The three gas sensors are all located in the same low temperature fumarole (LVY) within the fault zone. The temperature sensor is located within the same fumarole but close to the surface and therefore subject to external temperature influences. The temperature of the fumarole at the depth of the gas sensors is 93 °C.

FIGURE 12. Data for the period August 12 to September 27, 1985 from three reducing-gas sensors at monitoring site CDX. Sensor CDX1 is in a small boiling-temperature fumarole in the middle of the fault zone and altered area. Sensor CDX2 is in warm ground at the eastern edge of the altered area, and sensor CDX3 is in soil several meters east of the other sensors and out of the fault zone and altered area.

FIGURE 13. Data for the period August 12 to September 27, 1985 from three reducing-gas sensors at monitoring site CDY. Sensor CDY1 is in a 1 meter deep pit in hot clay in the center of the altered area and fault zone. Sensor CDY2 is in warm ground at the eastern edge of the altered area and CDY3 is in soil 50 m west of the fault zone.

FIGURE 14. Data for the period August 12 to September 27, 1985 from three reducing-gas sensors at monitoring site CDN. Sensors CDN1, CDN2, and CDN3 are installed in warm ground at a depth of 1 meter. The exact location of the fault zone at CDN is not clear but it is likely that CDN1 and CDN2 are in the fault zone while CDN3 is adjacent to it.

FIGURE 15. Data for the period August 12 to September 27, 1985 for one reducing-gas sensor (CDW7) buried 1 meter in cold soil at the weather station (CDW). CDW7 is located about 75 m east of the fault zone.

FIGURE 16. Air temperature, relative humidity, and rainfall in Long Valley caldera for the period August 12 to September 27, 1985. Air temperature and relative humidity are from monitoring station CDW while rainfall is from the U. S. Forest Service rain gauge at Mammoth Ranger Station.

FIGURE 17. Wind speed, wind direction, and barometric pressure for the period August 12 to September 27, 1985 from monitoring station CDW. Vertical axis for wind direction is compass direction from which wind is blowing.

FIGURE 18. Wind speed, air temperature, and gas data from three reducing-gas sensors (CDX1, CDN1, and LVY1) for a five-day period beginning September 18, 1985 showing a comparison of daily maxima and minima.

FIGURE 19. Barometric pressure, relative humidity, and gas data from three reducing-gas sensors (CDX1, CDN1, and LVY1) for a five-day period beginning September 18, 1985 showing a comparison of daily maxima and minima.

FIGURE 20. Wind direction, solar panel/battery voltage, and gas data from three reducing-gas sensors (CDX1, CDN1, and LVY1) for a five-day period beginning September 18, 1985. Notice the subdued diurnal features for battery-solar and wind direction during the first 40 hours of the time period and the corresponding lack of well developed diurnals for the three gas sensors during the same period.

FIGURE 21. Rainfall data, represented as vertical bars, superimposed on gas data from monitoring station LVY for the period August 12 to September 27, 1985.

FIGURE 22. Rainfall data, represented as vertical bars, superimposed on gas data from monitoring station CDX for the period August 12 to September 27, 1985.

FIGURE 23. Rainfall data, represented as vertical bars, superimposed on gas data from monitoring station CDY for the period August 12 to September 27, 1985.

FIGURE 24. Rainfall data, represented as vertical bars, superimposed on gas data from monitoring station CDN for the period August 12 to September 27, 1985.

FIGURE 25. Rainfall data, represented as vertical bars, superimposed on gas data from sensor CDW7 for the period August 12 to September 27, 1985.

FIGURE 26. Plot showing the relationship of seismicity local to Casa Diablo (vertical lines) with rainfall (vertical bars) for the period August 12 to September 27, 1985. Vertical scale is inches of rainfall.

FIGURE 27. Plot showing Long Valley caldera earthquakes (vertical lines) superimposed on gas data from station LVY for the period August 12 to September 27, 1985.

FIGURE 28. Plot showing Long Valley caldera earthquakes (vertical lines) superimposed on gas data from station CDX for the period August 12 to September 27, 1985.

FIGURE 29. Plot showing Long Valley caldera earthquakes (vertical lines) superimposed on gas data from station CDY for the period August 12 to September 27, 1985.

FIGURE 30. Plot showing Long Valley caldera earthquakes (vertical lines) superimposed on gas data from station CDN for the period August 12 to September 27, 1985.

FIGURE 31. Plot showing Long Valley caldera earthquakes (vertical lines) superimposed on gas data from sensor CDW7 for the period August 12 to September 27, 1985.

FIGURE 32. Plot showing earth tides superimposed on gas data from station LVY for the period August 12 to September 27, 1985.

FIGURE 33. Plot showing earth tides superimposed on gas data from station CDX for the period August 12 to September 27, 1985.

FIGURE 34. Plot showing earth tides superimposed on gas data from station CDY for the period August 12 to September 27, 1985.

FIGURE 35. Plot showing earth tides superimposed on gas data from station CDN for the period August 12 to September 27, 1985.

FIGURE 36. Plot showing earth tides superimposed on gas data from senso CDW7 for the period August 12 to September 27, 1985.

FIGURE 37. Plot showing hydrogen content of fumaroles LVY, MCF, and LCD for a 24-hour period beginning September 24, 1985. Hydrogen was analyzed by gas chromatography.

INTERNAL RESISTANCE

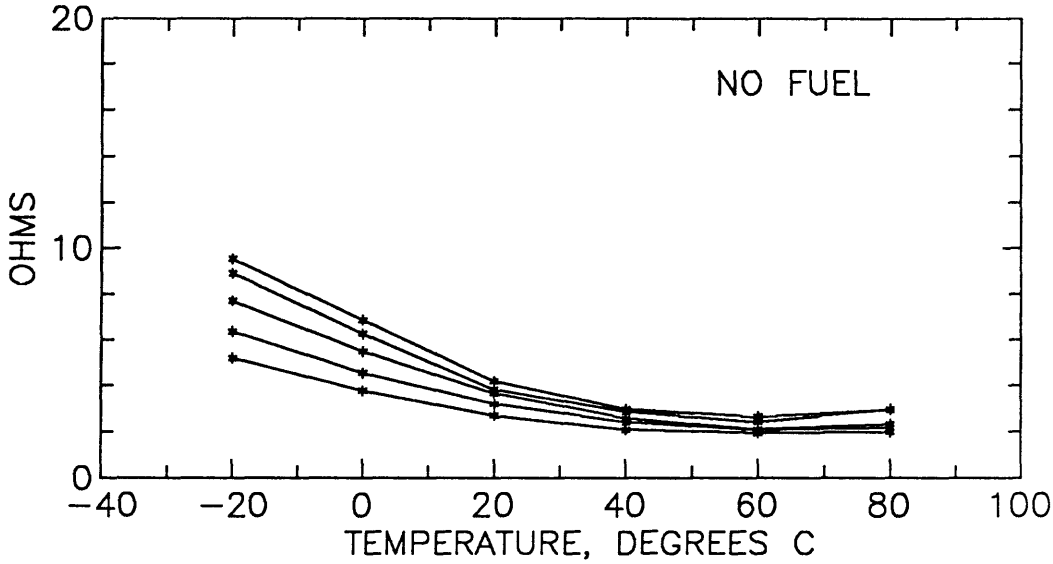

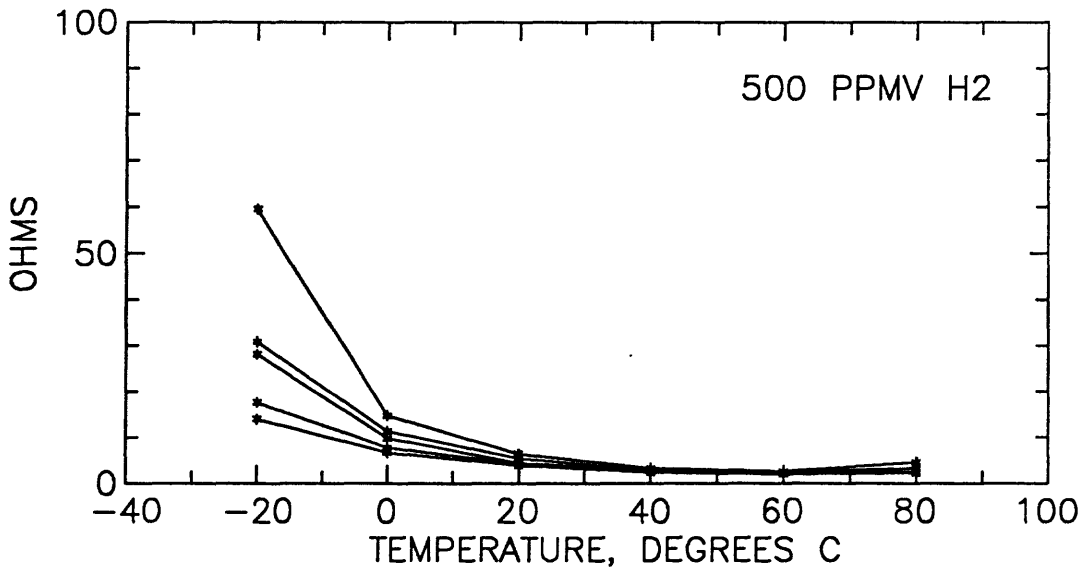

FIGURE 2.

REDUCING GAS SENSOR

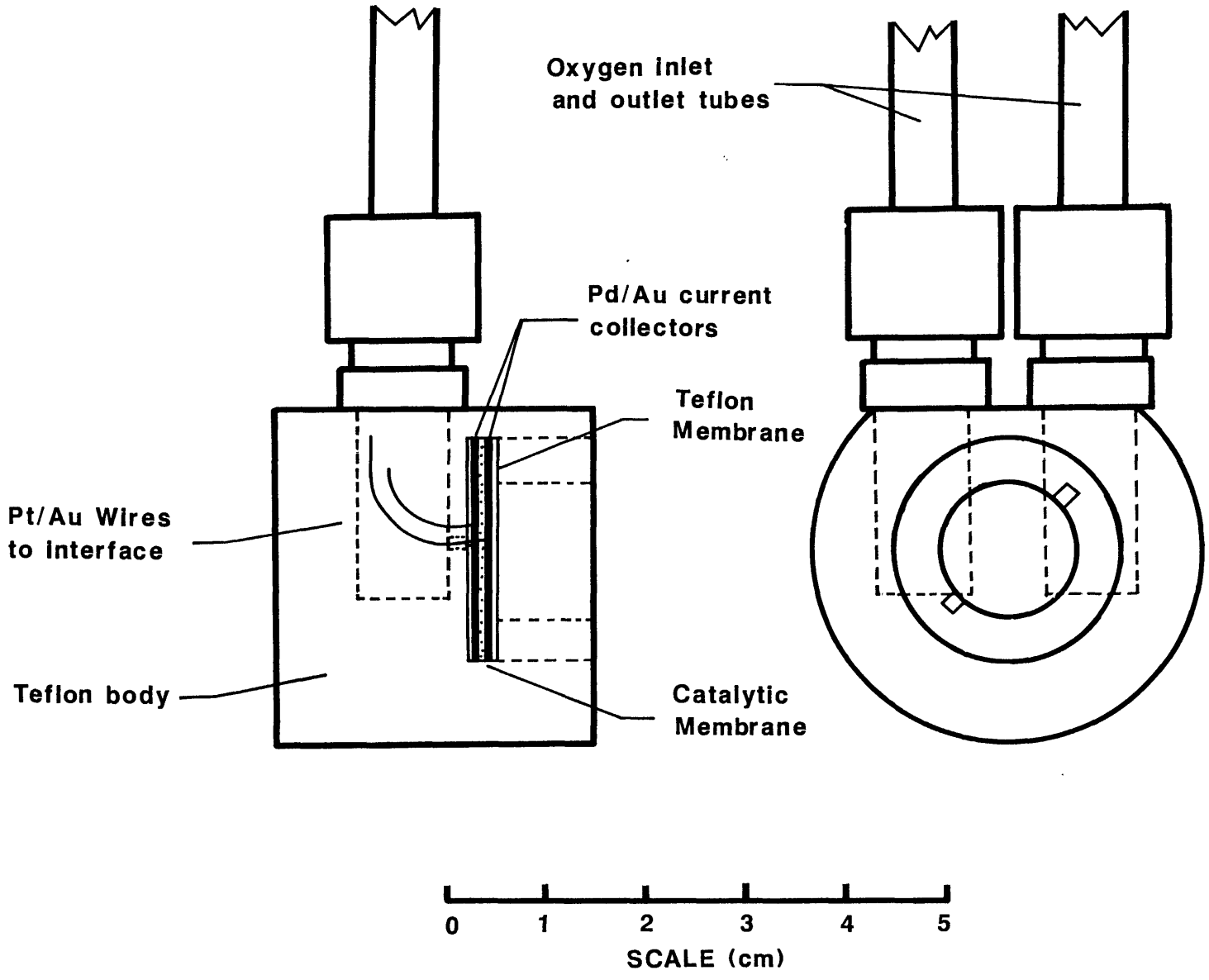

FIGURE 1.

LOAD RESISTANCE

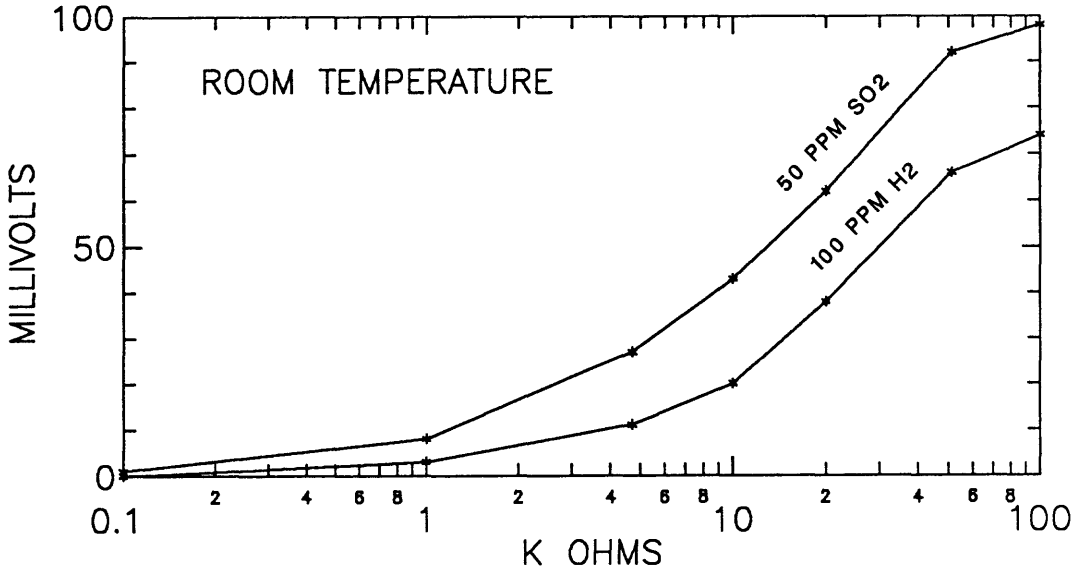

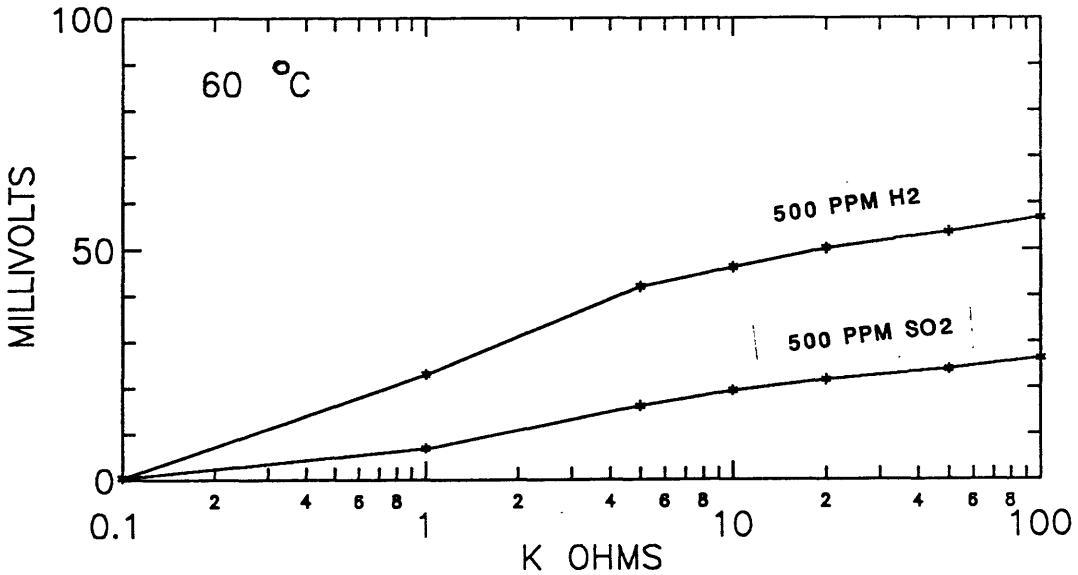

FIGURE 3.

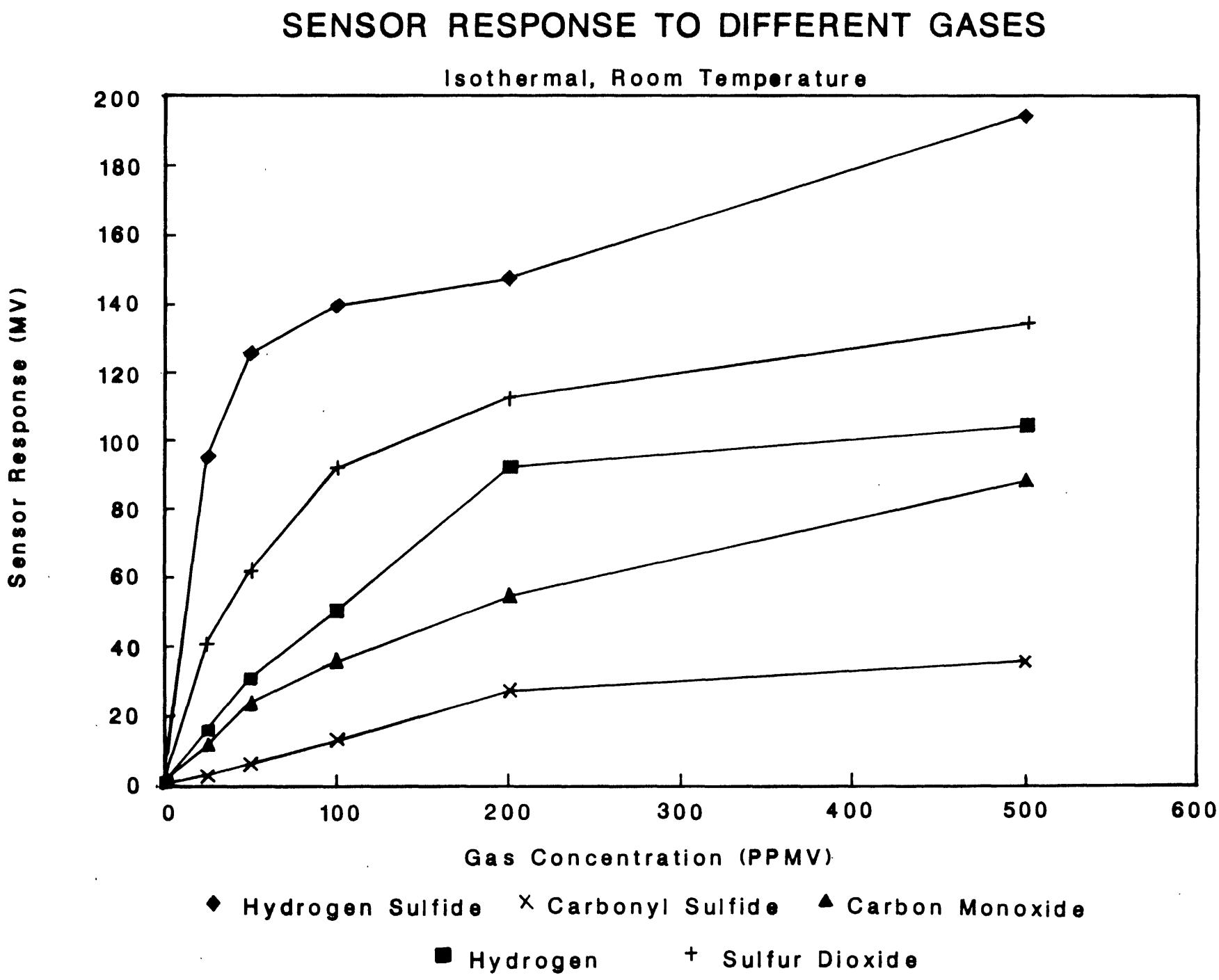
SENSOR RESPONSE TO DIFFERENT GASES
Isothermal, Room Temperature
Sensor Response (MV)
200
180
160
140
120
100
80
60
40
20
0
0
100
200
300
400
500
600
Gas Concentration (PPMV)
Hydrogen Sulfide
Carbonyl Sulfide
Carbon Monoxide
Hydrogen
Sulfur Dioxide

FIGURE 4.

HYDROGEN SULFIDE

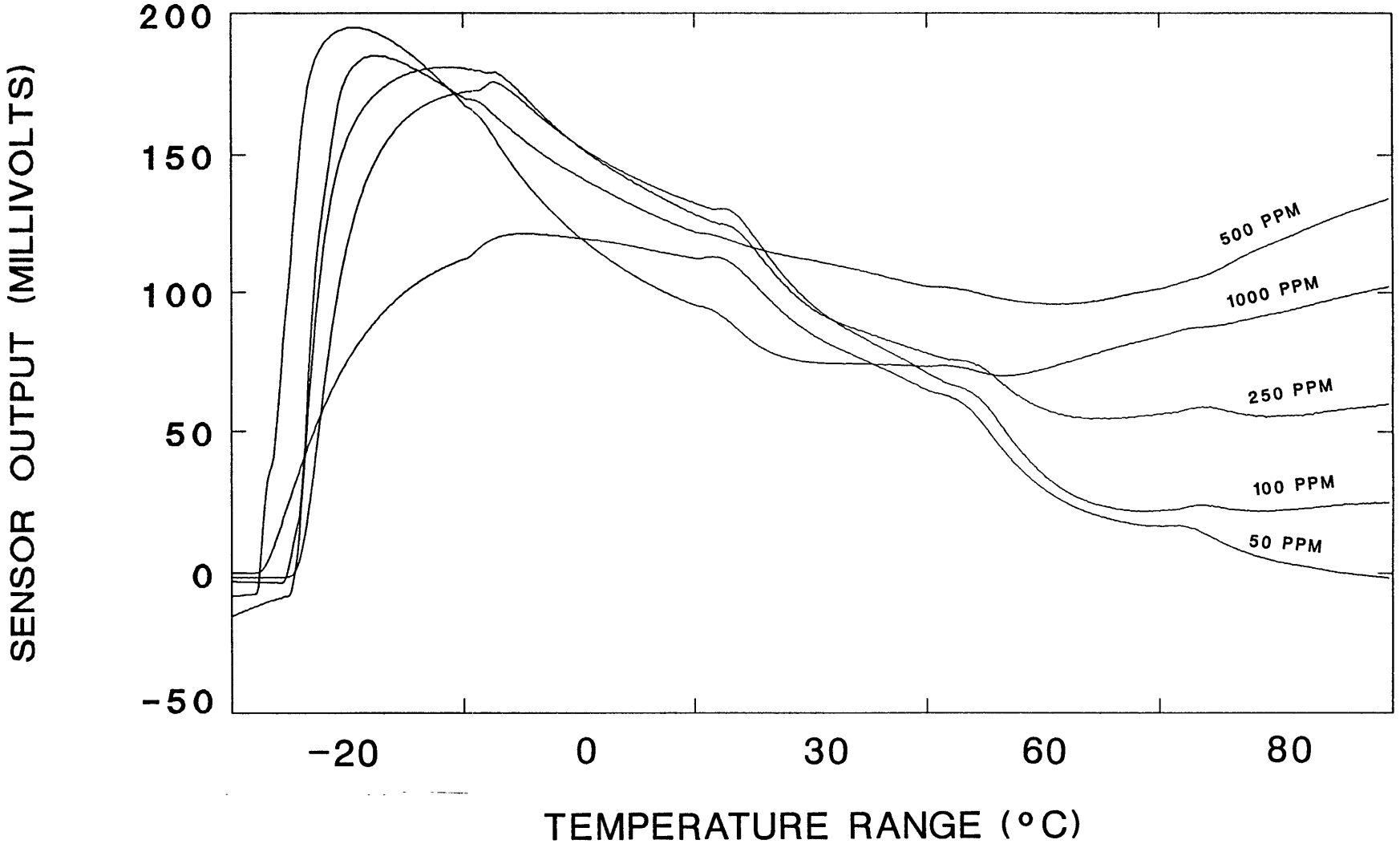

FIGURE 5.

SULFUR DIOXIDE

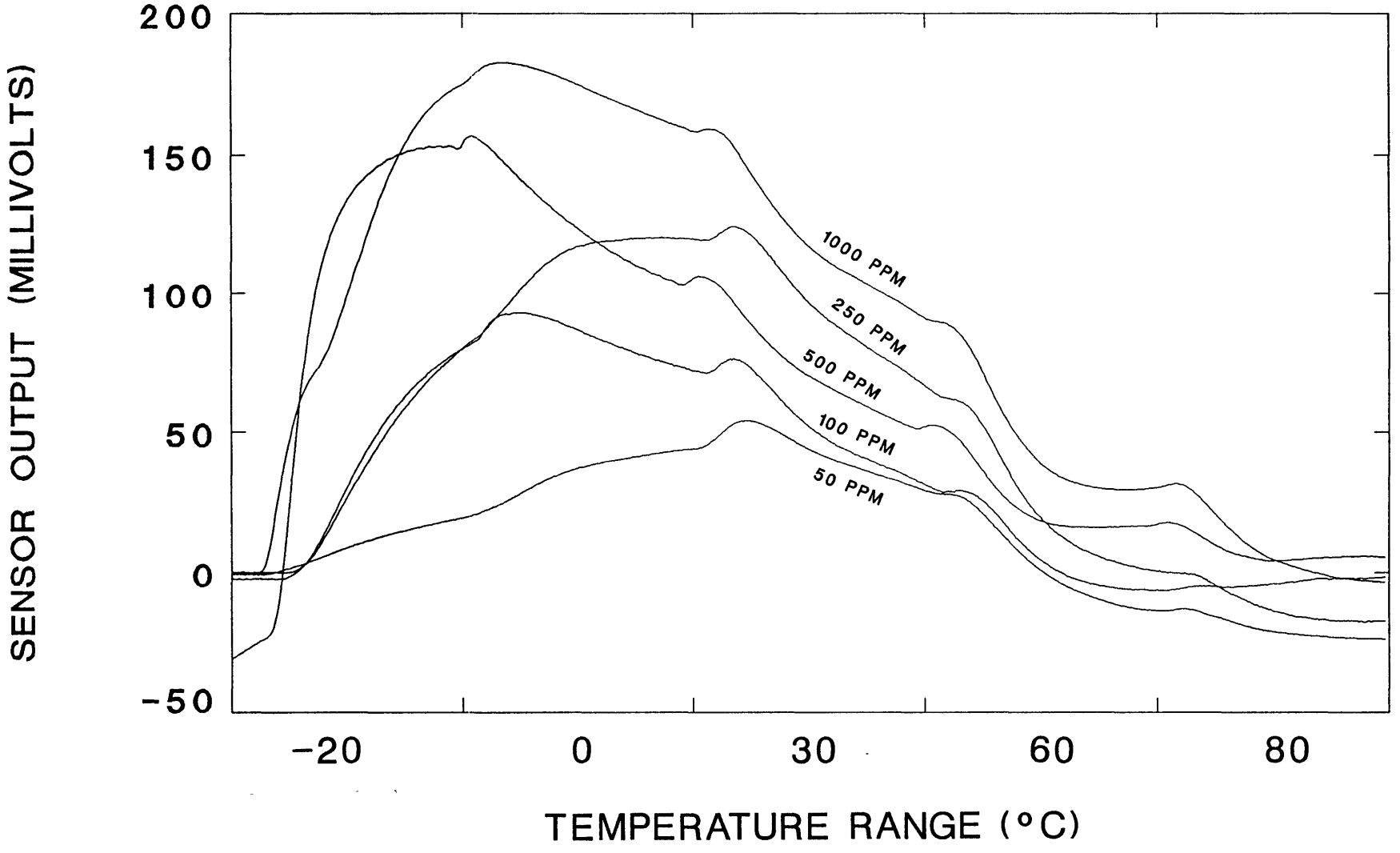

FIGURE 6.

HYDROGEN

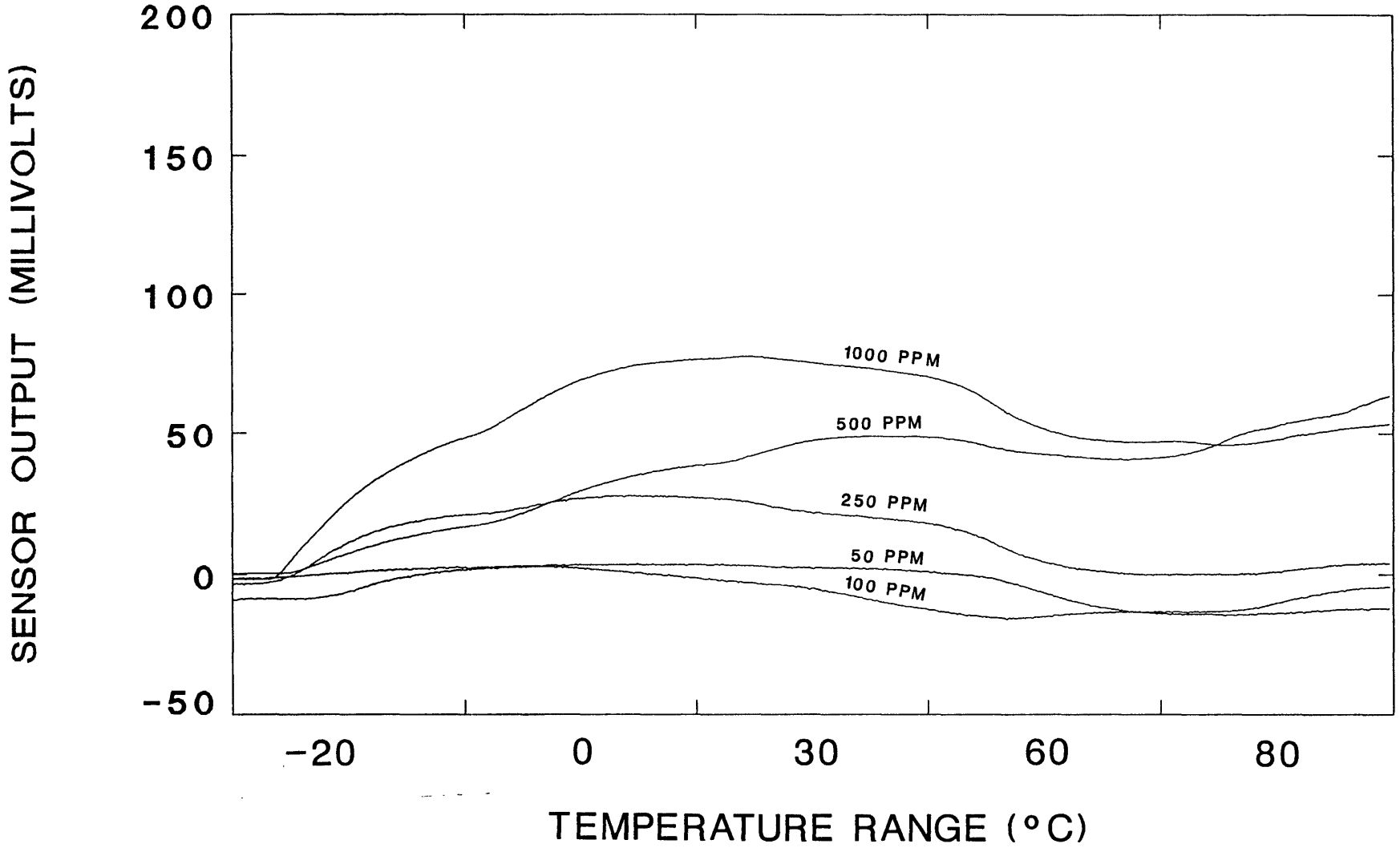

FIGURE 7.

CARBON MONOXIDE

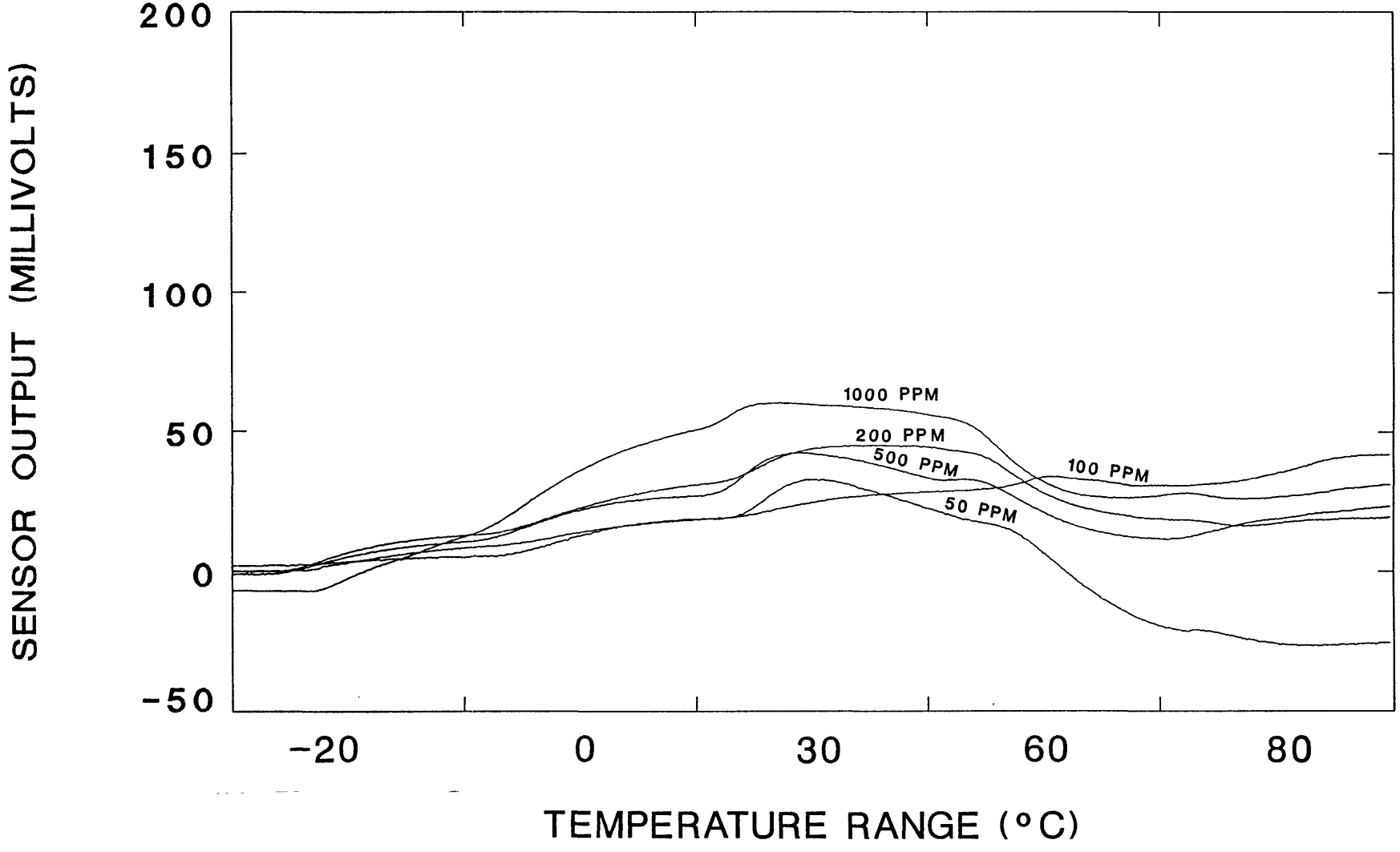

FIGURE 8.

CARBONYL SULFIDE

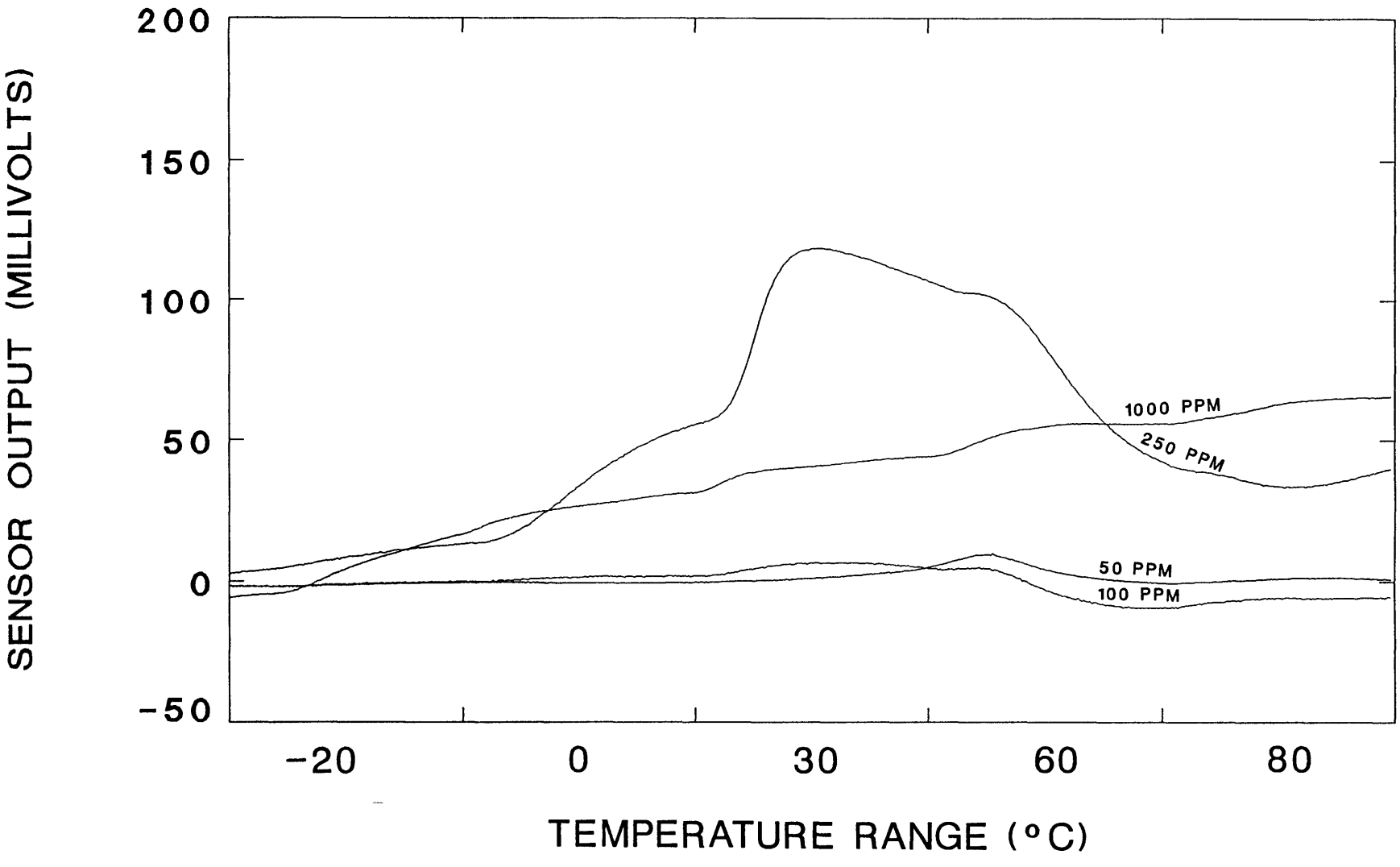

FIGURE 9.

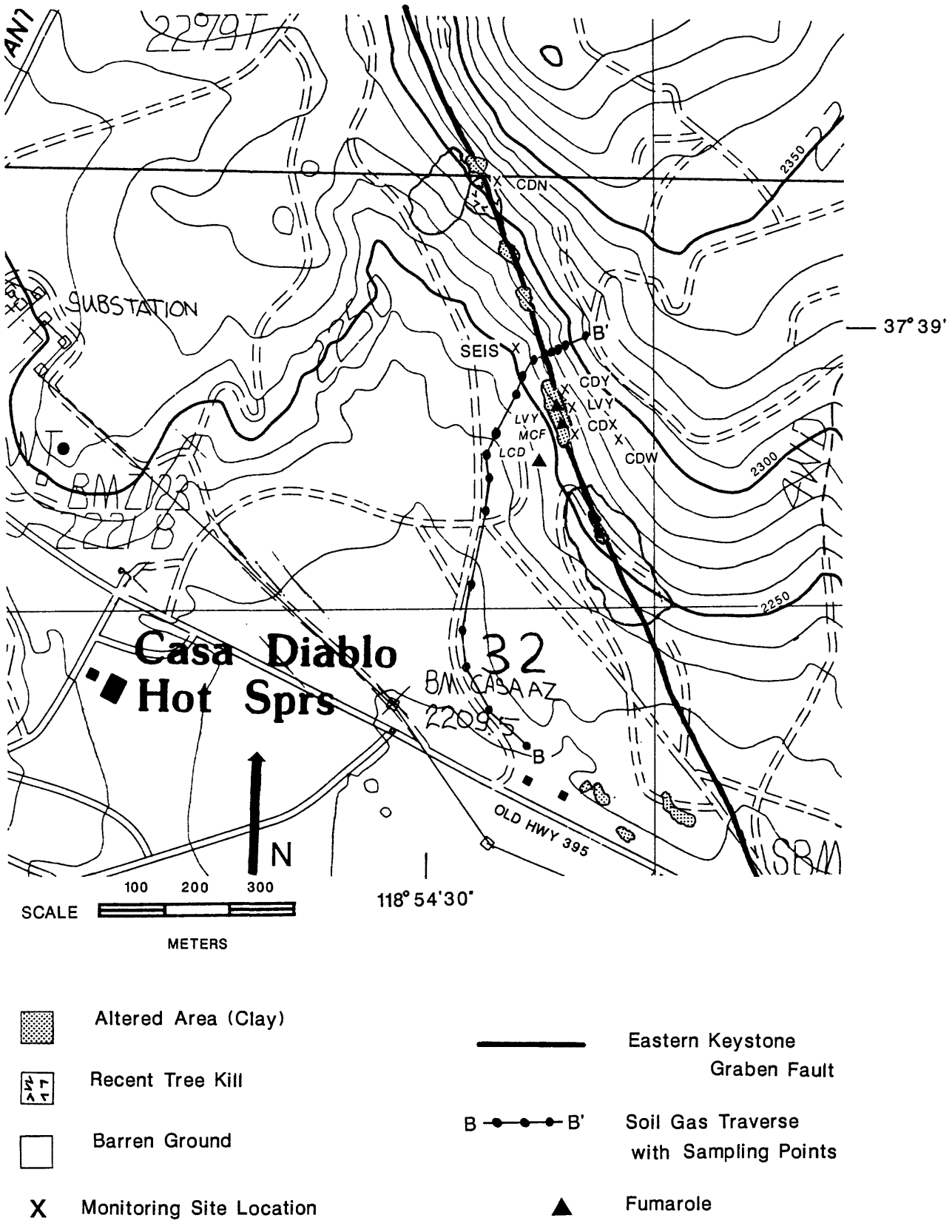
2279T
SUBSTATION
CDN
SEIS
B'
CDY
LVY
CDX
CDW
LVY
MCF
LCD
2350
2300
2250
37°39'
Casa Diablo
Hot Sprs
32
BM CASA AZ
2209.5
B
OLD HWY 395
N
100 200 300
SCALE
METERS
118°54'30"
Altered Area (Clay)
Recent Tree Kill
Barren Ground
X Monitoring Site Location
Eastern Keystone Graben Fault
B B' Soil Gas Traverse with Sampling Points
Fumarole

FIGURE 10.

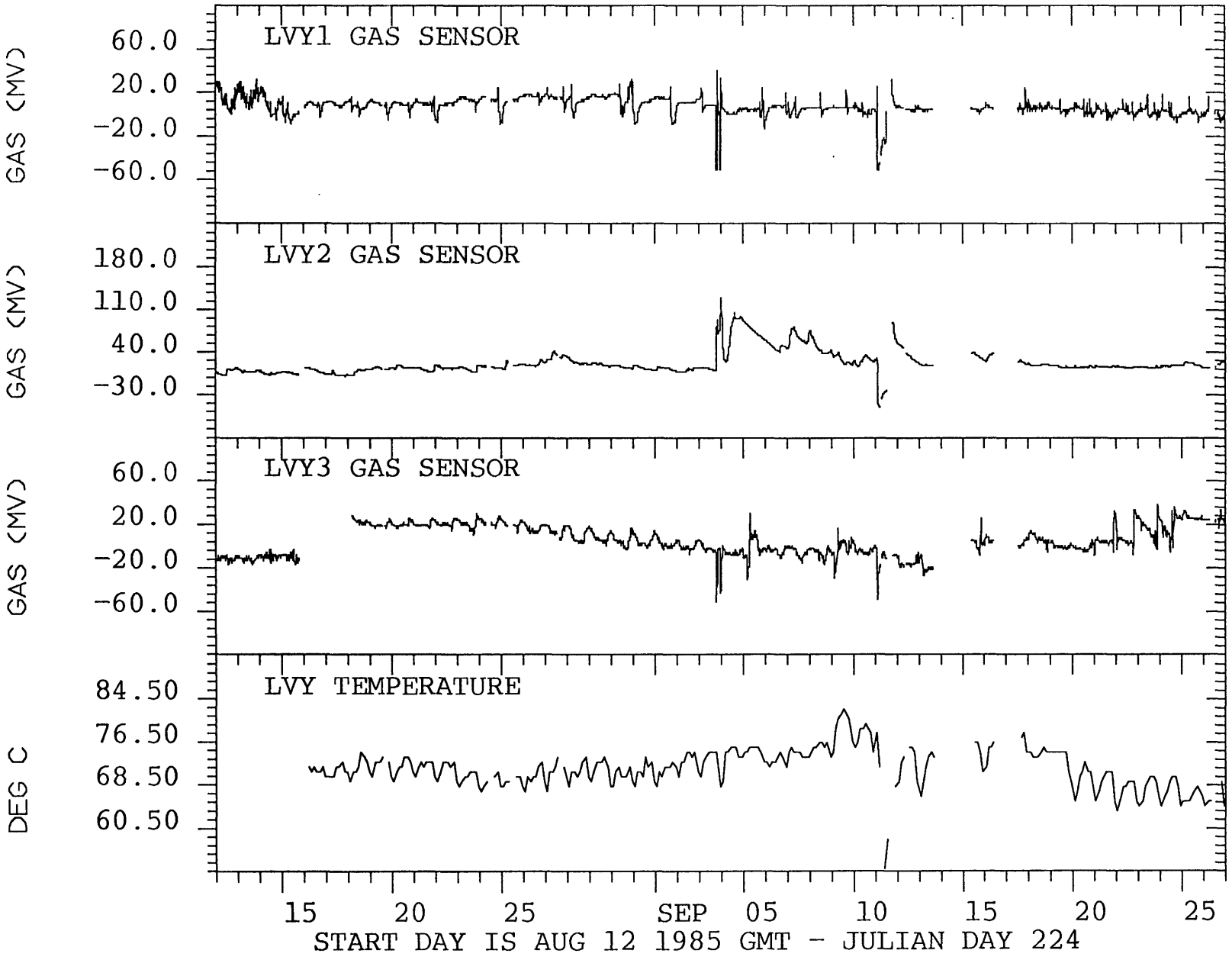
LVY1 GAS SENSOR
60.0
20.0
-20.0
-60.0
GAS (MV)
LVY2 GAS SENSOR
180.0
110.0
40.0
-30.0
GAS (MV)
LVY3 GAS SENSOR
60.0
20.0
-20.0
-60.0
GAS (MV)
LVY TEMPERATURE
84.50
76.50
68.50
60.50
DEG C
15
20
25
SEP
05
10
15
20
25
START DAY IS AUG 12 1985 GMT - JULIAN DAY 224

FIGURE 11.

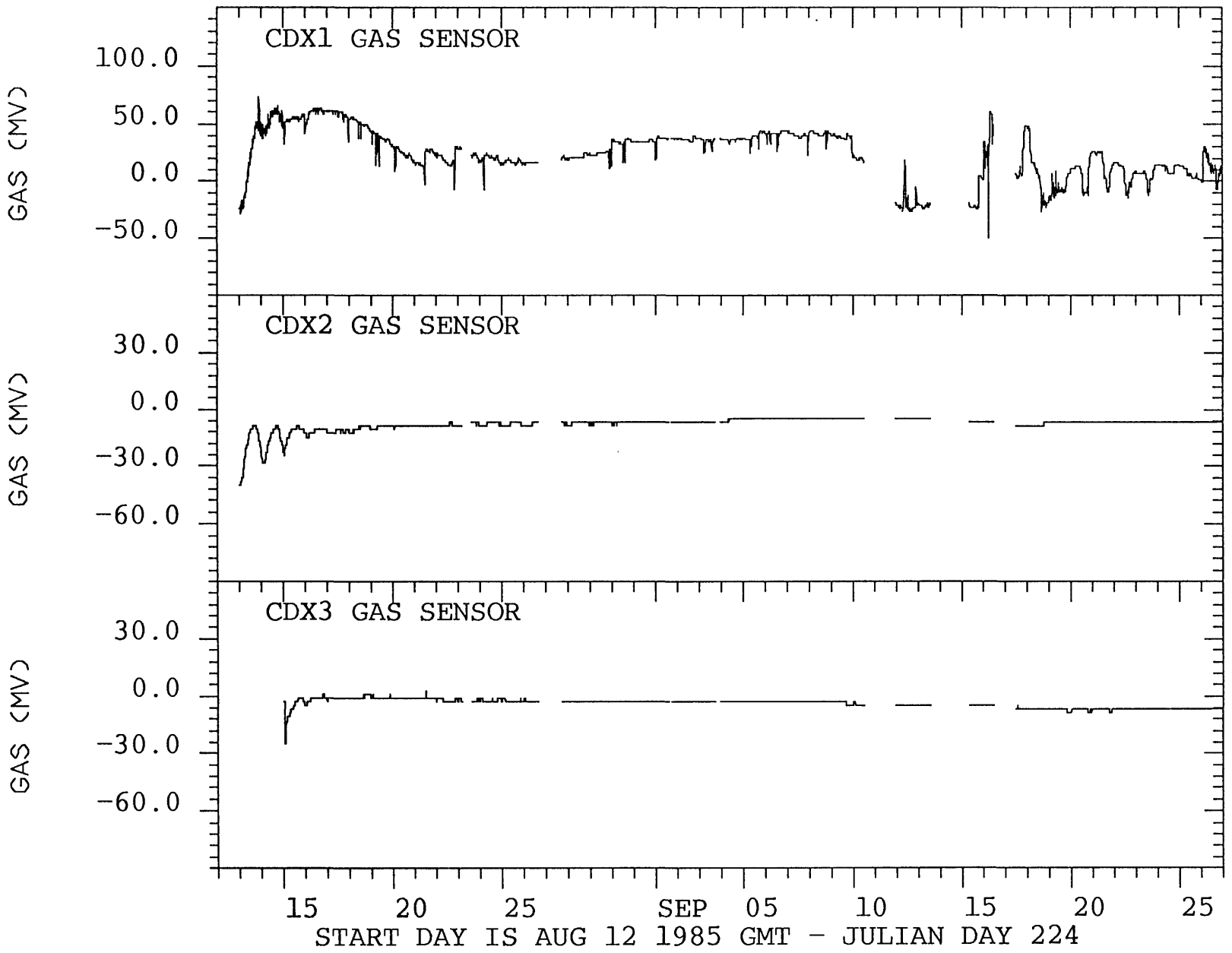
CDX1 GAS SENSOR
100.0
50.0
0.0
-50.0
GAS (MV)
CDX2 GAS SENSOR
30.0
0.0
-30.0
-60.0
GAS (MV)
CDX3 GAS SENSOR
30.0
0.0
-30.0
-60.0
GAS (MV)
15
20
25
SEP
05
10
15
20
25
START DAY IS AUG 12 1985 GMT - JULIAN DAY 224

FIGURE 12.

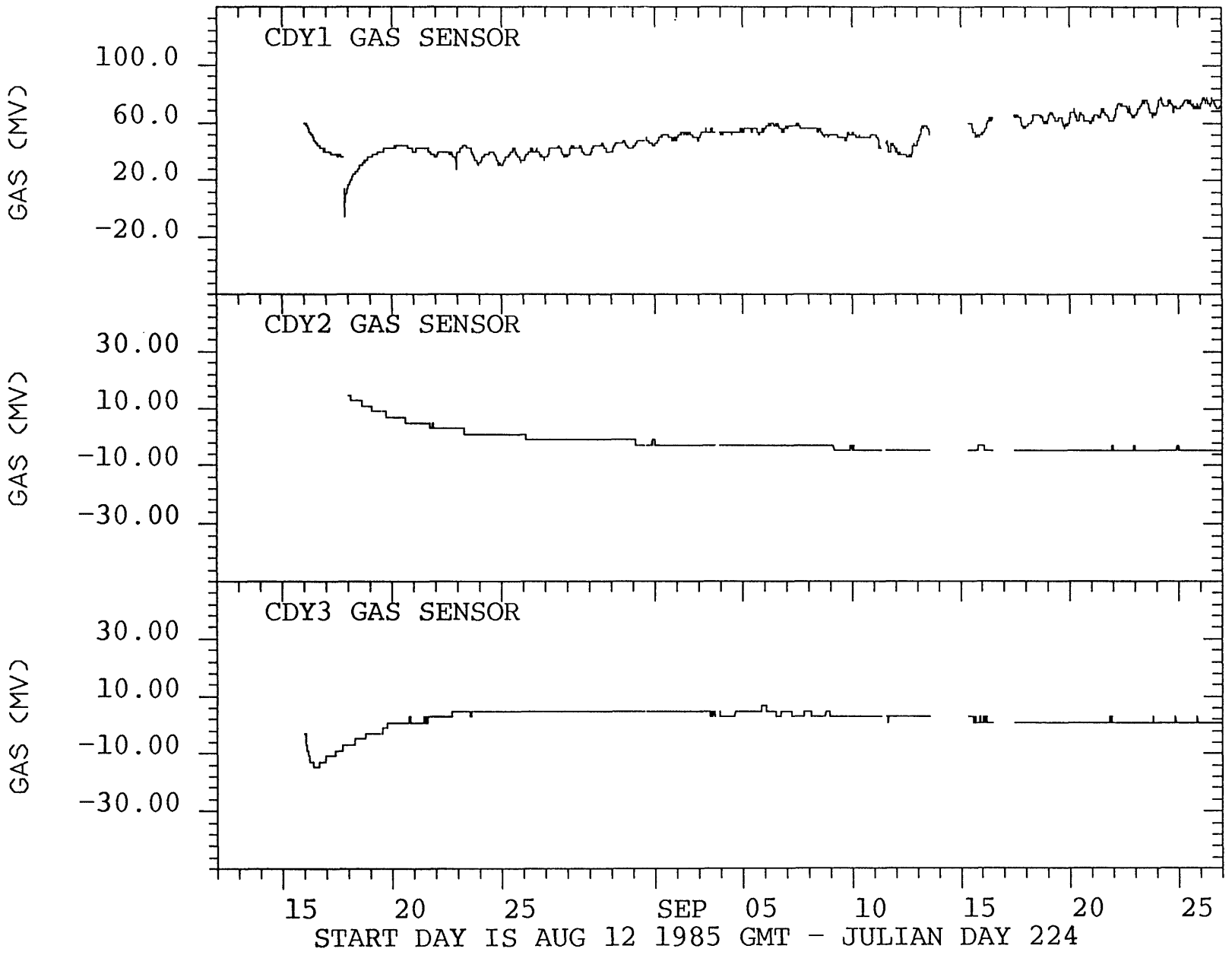
CDY1 GAS SENSOR
100.0
60.0
20.0
-20.0
GAS (MV)
CDY2 GAS SENSOR
30.00
10.00
-10.00
-30.00
GAS (MV)
CDY3 GAS SENSOR
30.00
10.00
-10.00
-30.00
GAS (MV)
15
20
25
SEP
05
10
15
20
25
START DAY IS AUG 12 1985 GMT - JULIAN DAY 224

FIGURE 13.

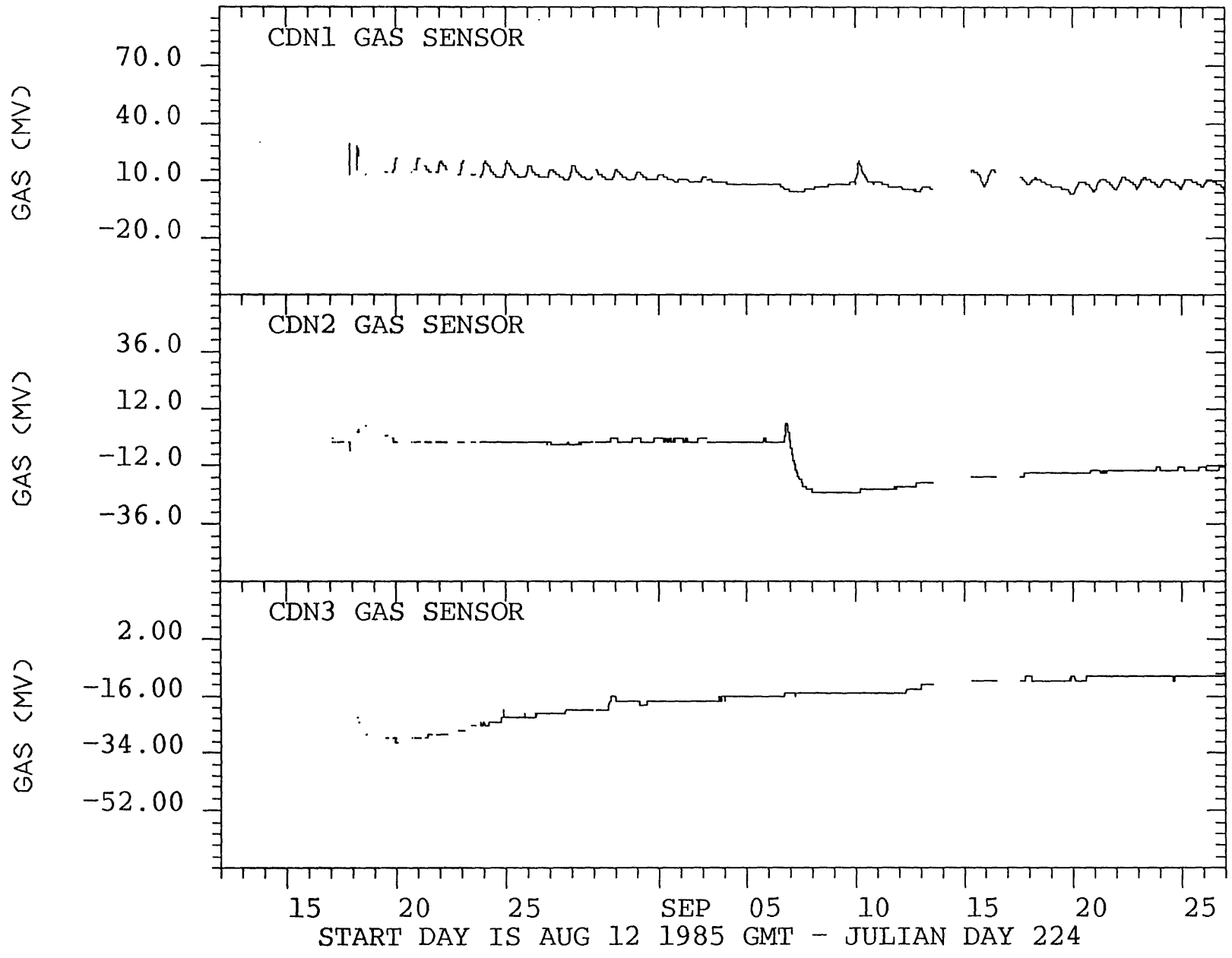
CDN1 GAS SENSOR
70.0
40.0
10.0
-20.0
GAS (MV)
CDN2 GAS SENSOR
36.0
12.0
-12.0
-36.0
GAS (MV)
CDN3 GAS SENSOR
2.00
-16.00
-34.00
-52.00
GAS (MV)
15
20
25
SEP
05
10
15
20
25
START DAY IS AUG 12 1985 GMT - JULIAN DAY 224

FIGURE 14.

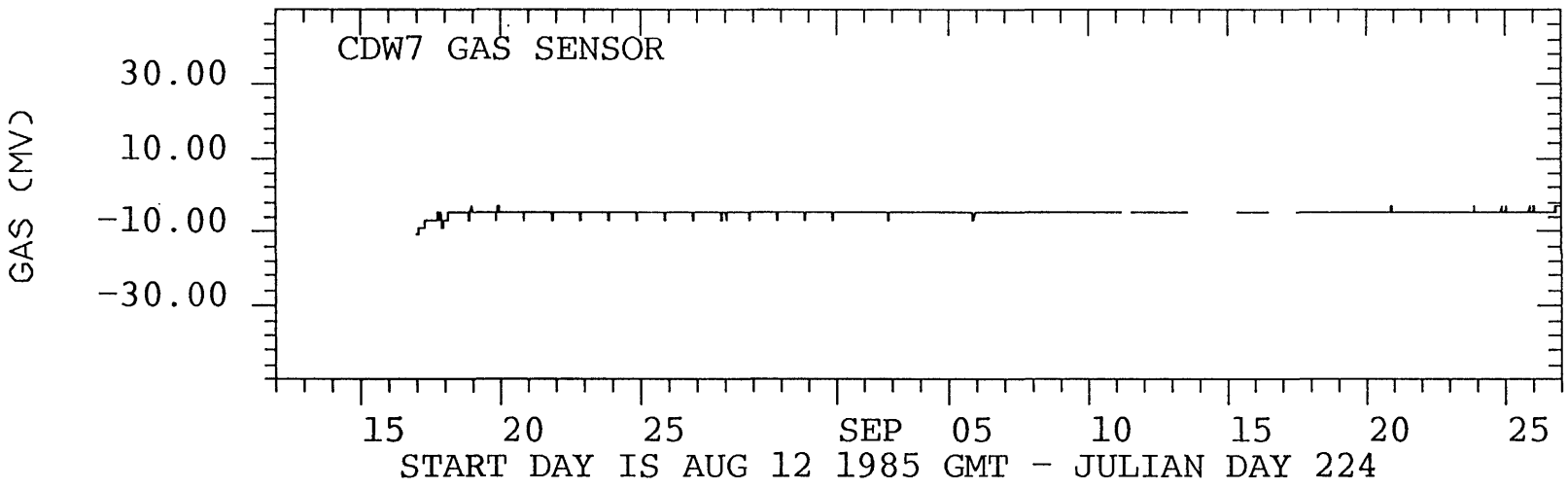
CDW7 GAS SENSOR
GAS (MV)
30.00
10.00
-10.00
-30.00
15
20
25
SEP
05
10
15
20
25
START DAY IS AUG 12 1985 GMT - JULIAN DAY 224

FIGURE 15.

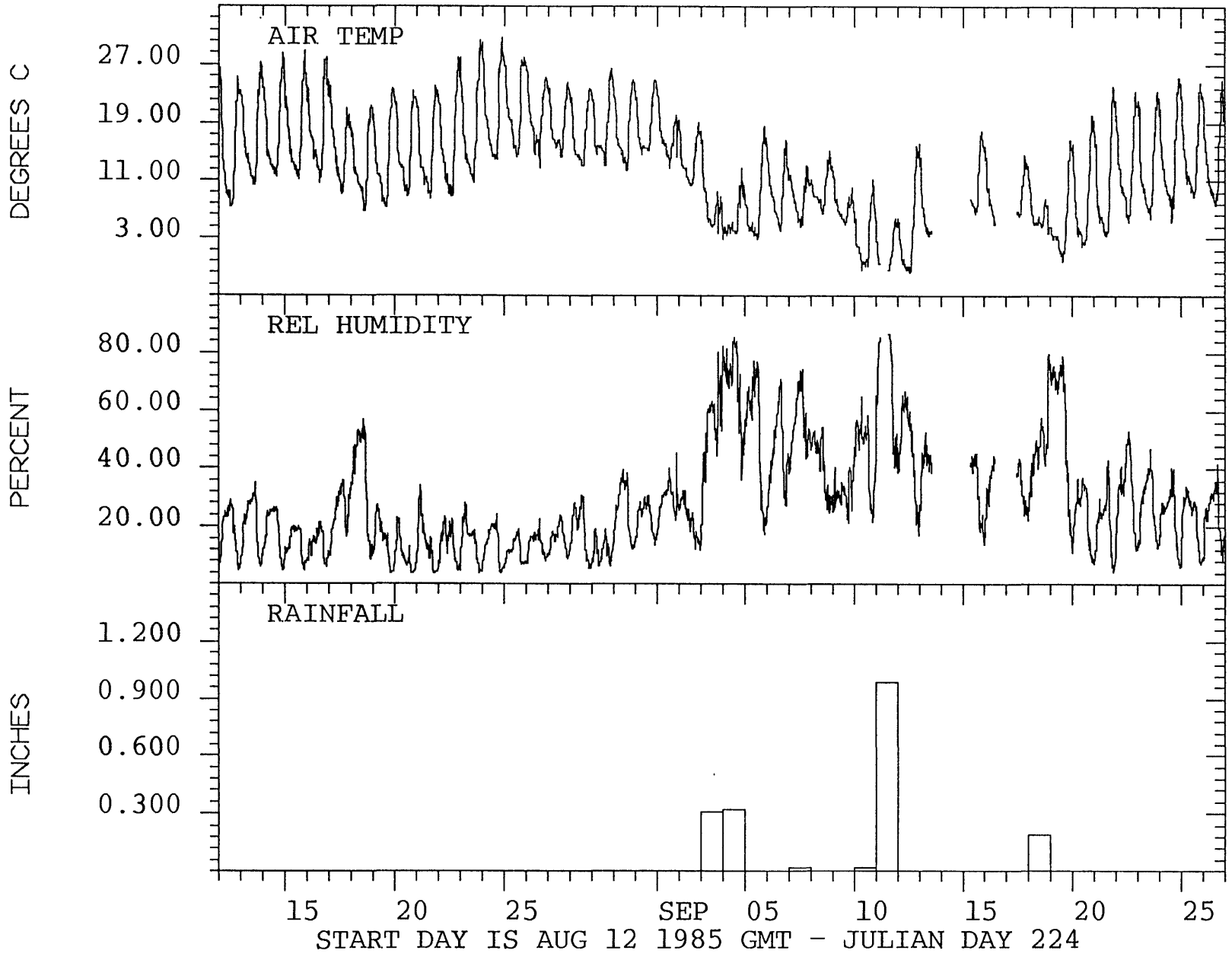
AIR TEMP
DEGREES C
27.00
19.00
11.00
3.00
REL HUMIDITY
PERCENT
80.00
60.00
40.00
20.00
RAINFALL
INCHES
1.200
0.900
0.600
0.300
15
20
25
SEP
05
10
15
20
25
START DAY IS AUG 12 1985 GMT - JULIAN DAY 224

FIGURE 16.

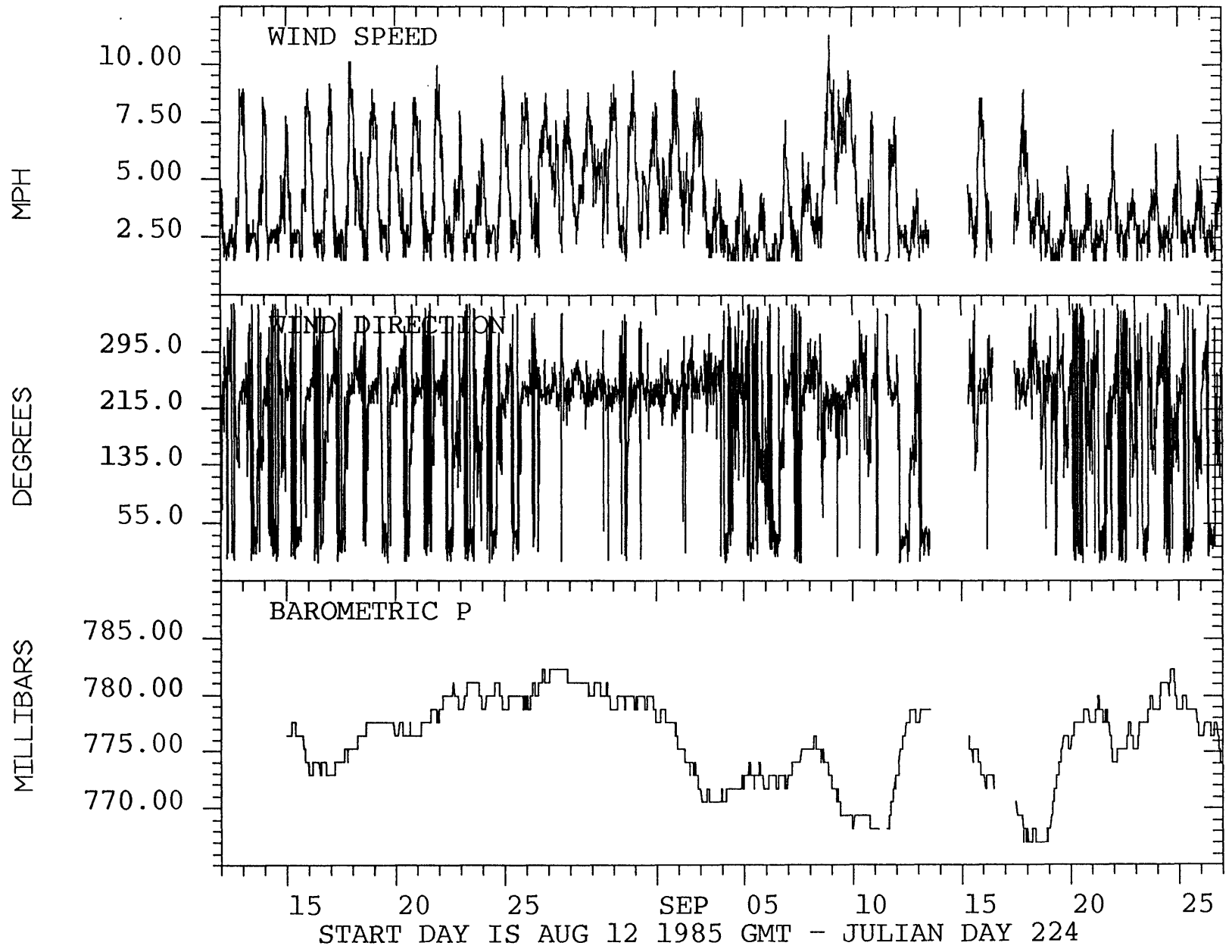
WIND SPEED
10.00
7.50
5.00
2.50
MPH
WIND DIRECTION
295.0
215.0
135.0
55.0
DEGREES
BAROMETRIC P
785.00
780.00
775.00
770.00
MILLIBARS
15
20
25
SEP
05
10
15
20
25
START DAY IS AUG 12 1985 GMT - JULIAN DAY 224

FIGURE 17.

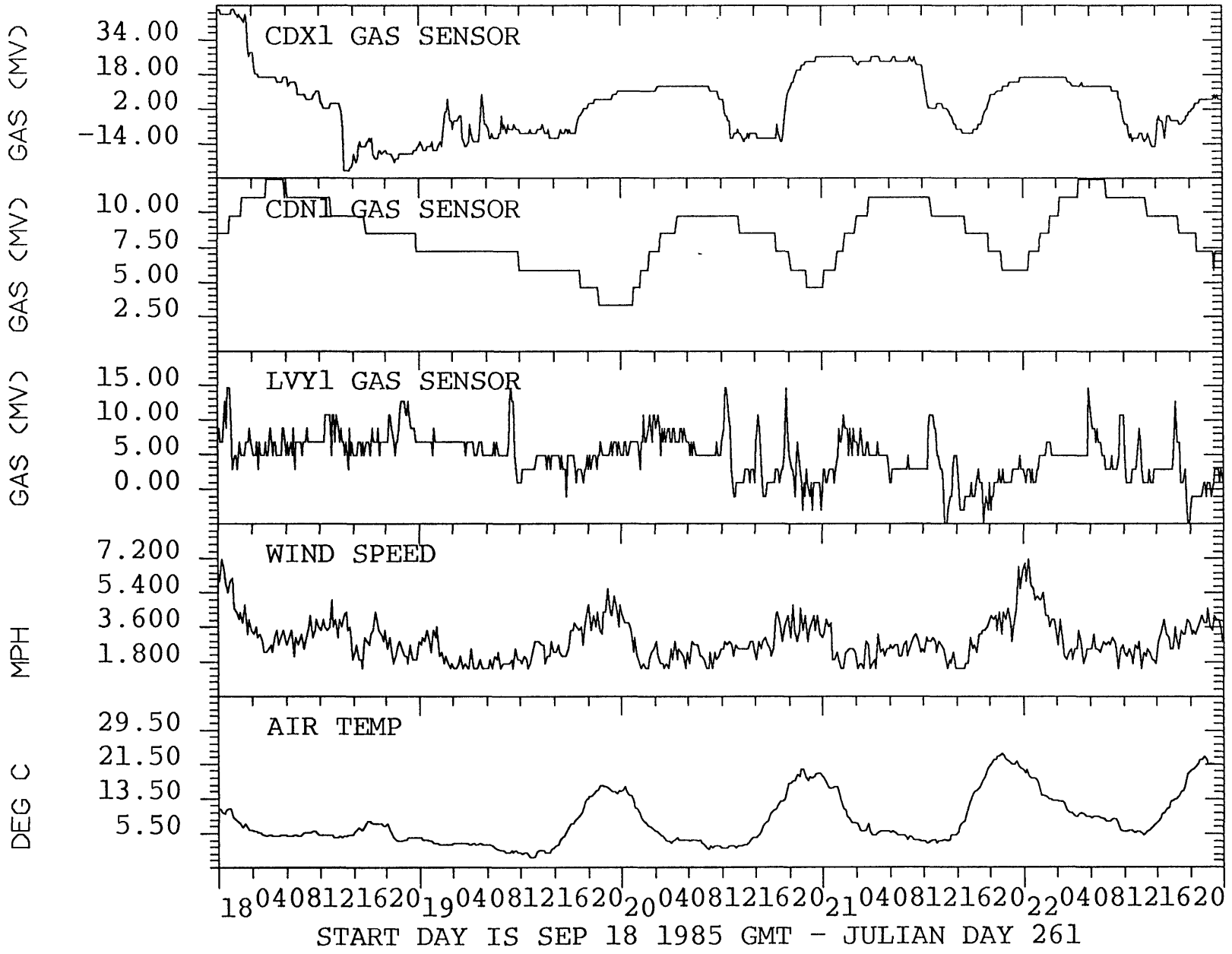
GAS (MV)
34.00
18.00
2.00
-14.00
CDX1 GAS SENSOR
GAS (MV)
10.00
7.50
5.00
2.50
CDN1 GAS SENSOR
GAS (MV)
15.00
10.00
5.00
0.00
LVY1 GAS SENSOR
MPH
7.200
5.400
3.600
1.800
WIND SPEED
DEG C
29.50
21.50
13.50
5.50
AIR TEMP
18 04 08 12 16 20 19 04 08 12 16 20 20 04 08 12 16 20 21 04 08 12 16 20 22 04 08 12 16 20
START DAY IS SEP 18 1985 GMT - JULIAN DAY 261

FIGURE 18.

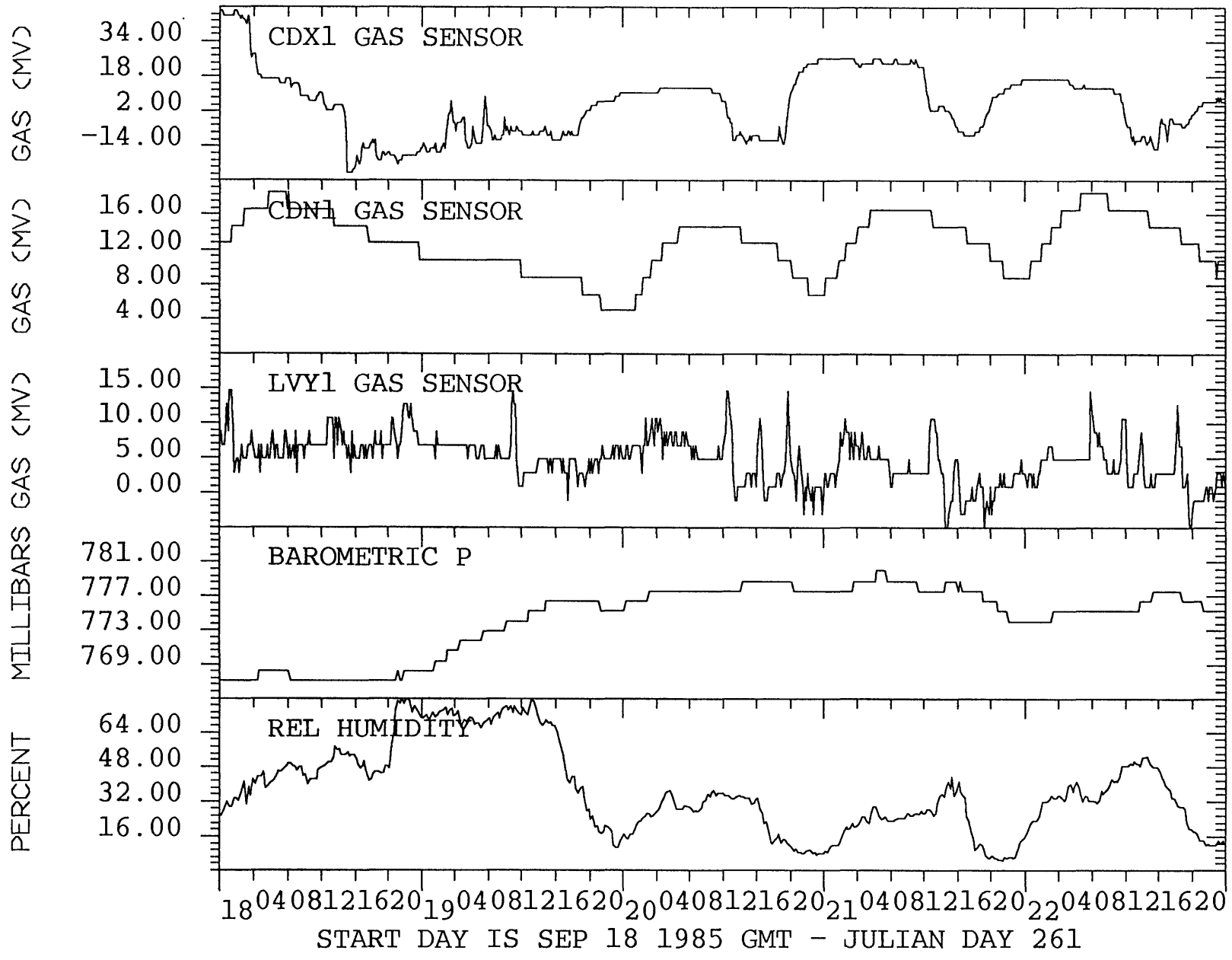
CDX1 GAS SENSOR
CDN1 GAS SENSOR
LVY1 GAS SENSOR
BAROMETRIC P
REL HUMIDITY
34.00
18.00
2.00
-14.00
16.00
12.00
8.00
4.00
15.00
10.00
5.00
0.00
781.00
777.00
773.00
769.00
64.00
48.00
32.00
16.00
PERCENT MILLIBARS GAS (MV) GAS (MV) GAS (MV) GAS (MV)
18 04 08 12 16 20 19 04 08 12 16 20 20 04 08 12 16 20 21 04 08 12 16 20 22 04 08 12 16 20
START DAY IS SEP 18 1985 GMT - JULIAN DAY 261

FIGURE 19.

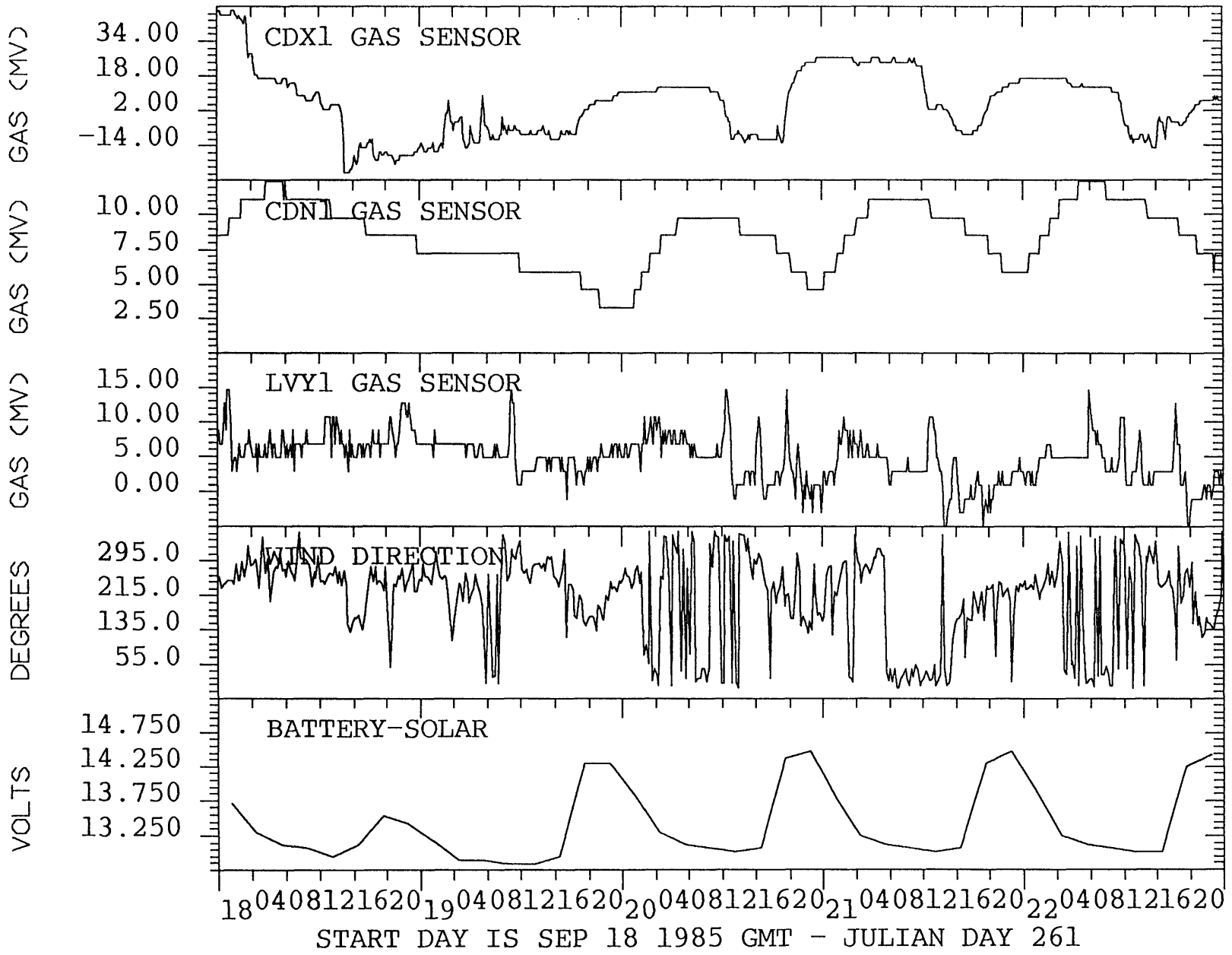
CDX1 GAS SENSOR
34.00
18.00
2.00
-14.00
GAS (MV)
CDN1 GAS SENSOR
10.00
7.50
5.00
2.50
GAS (MV)
LVY1 GAS SENSOR
15.00
10.00
5.00
0.00
GAS (MV)
WIND DIRECTION
295.0
215.0
135.0
55.0
DEGREES
BATTERY-SOLAR
14.750
14.250
13.750
13.250
VOLTS
18 0408121620 19 0408121620 20 0408121620 21 0408121620 22 0408121620
START DAY IS SEP 18 1985 GMT - JULIAN DAY 261

FIGURE 20.

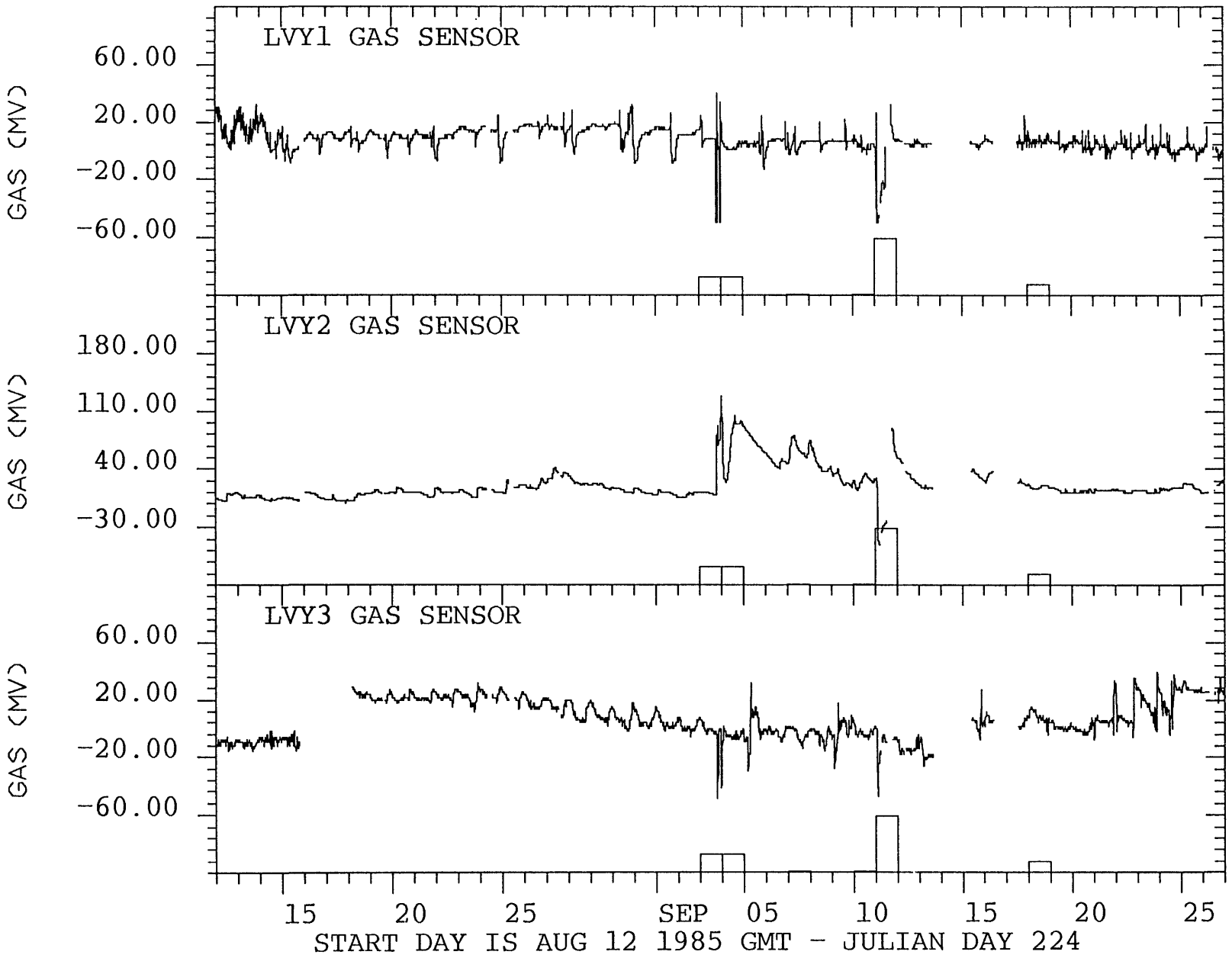
LVY1 GAS SENSOR
60.00
20.00
-20.00
-60.00
GAS (MV)
LVY2 GAS SENSOR
180.00
110.00
40.00
-30.00
GAS (MV)
LVY3 GAS SENSOR
60.00
20.00
-20.00
-60.00
GAS (MV)
15
20
25
SEP
05
10
15
20
25
START DAY IS AUG 12 1985 GMT - JULIAN DAY 224

FIGURE 21.

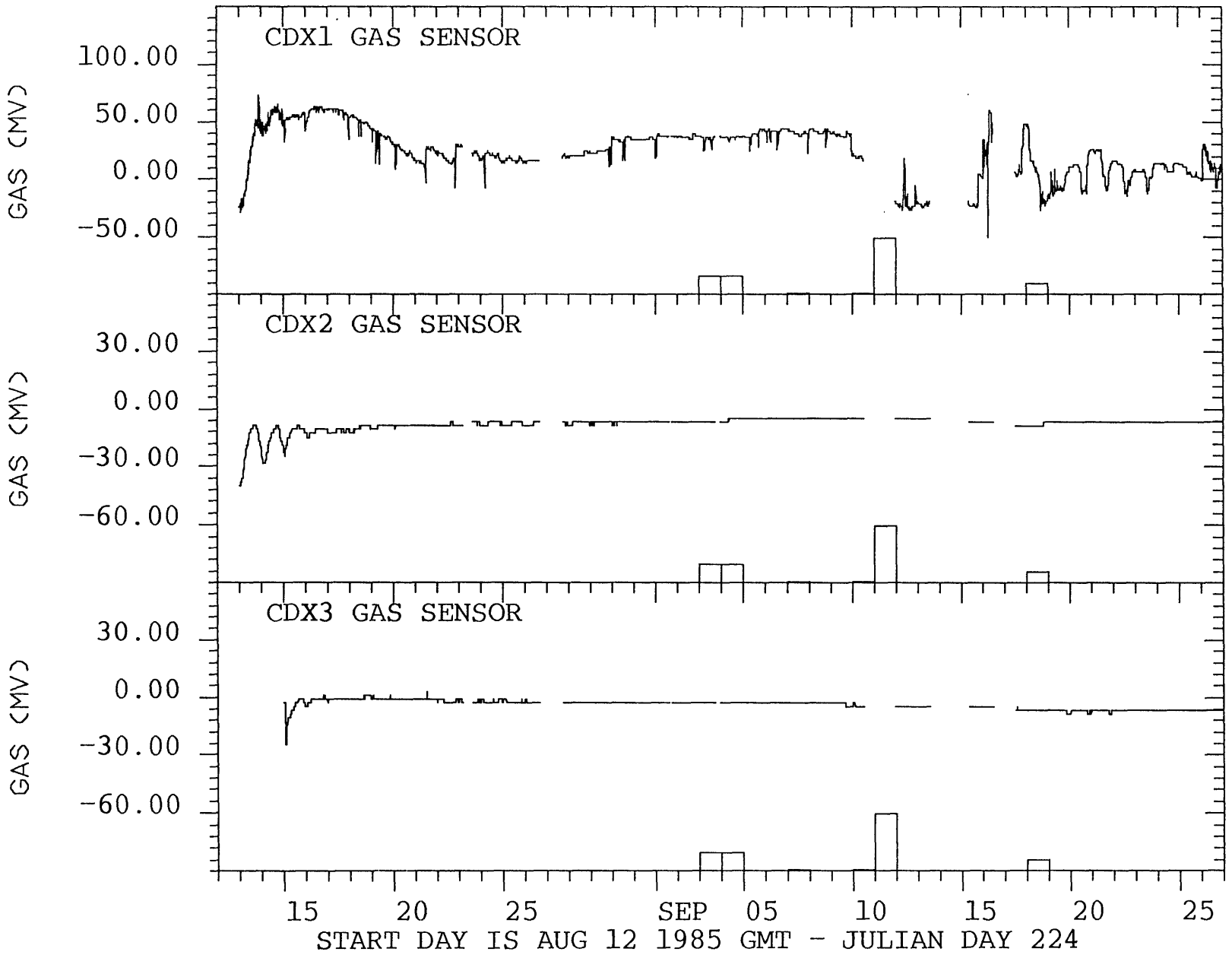
CDX1 GAS SENSOR
100.00
50.00
0.00
-50.00
GAS (MV)
CDX2 GAS SENSOR
30.00
0.00
-30.00
-60.00
GAS (MV)
CDX3 GAS SENSOR
30.00
0.00
-30.00
-60.00
GAS (MV)
15
20
25
SEP
05
10
15
20
25
START DAY IS AUG 12 1985 GMT - JULIAN DAY 224

FIGURE 22.

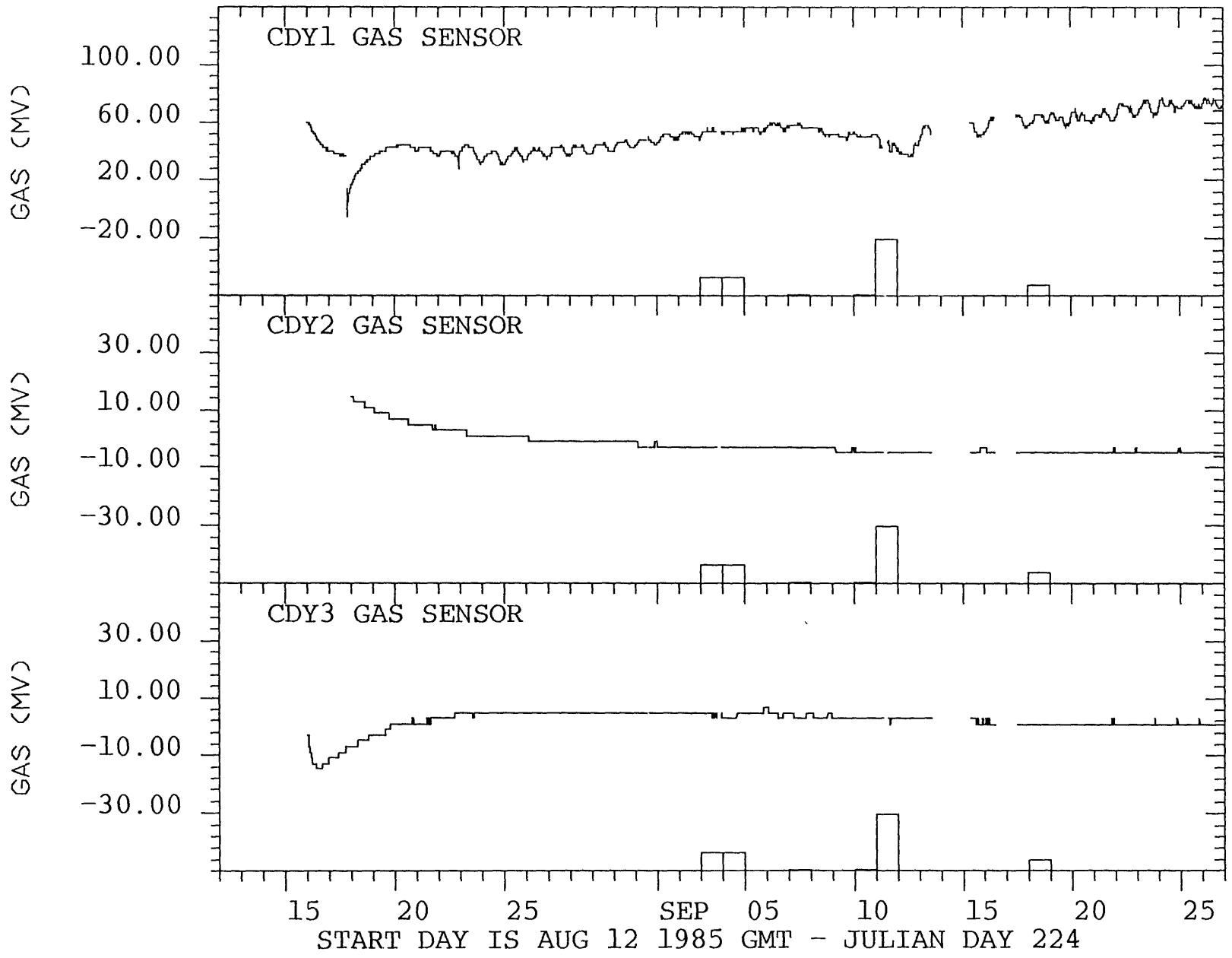
CDY1 GAS SENSOR
100.00
60.00
20.00
-20.00
GAS (MV)
CDY2 GAS SENSOR
30.00
10.00
-10.00
-30.00
GAS (MV)
CDY3 GAS SENSOR
30.00
10.00
-10.00
-30.00
GAS (MV)
15
20
25
SEP
05
10
15
20
25
START DAY IS AUG 12 1985 GMT - JULIAN DAY 224

FIGURE 23.

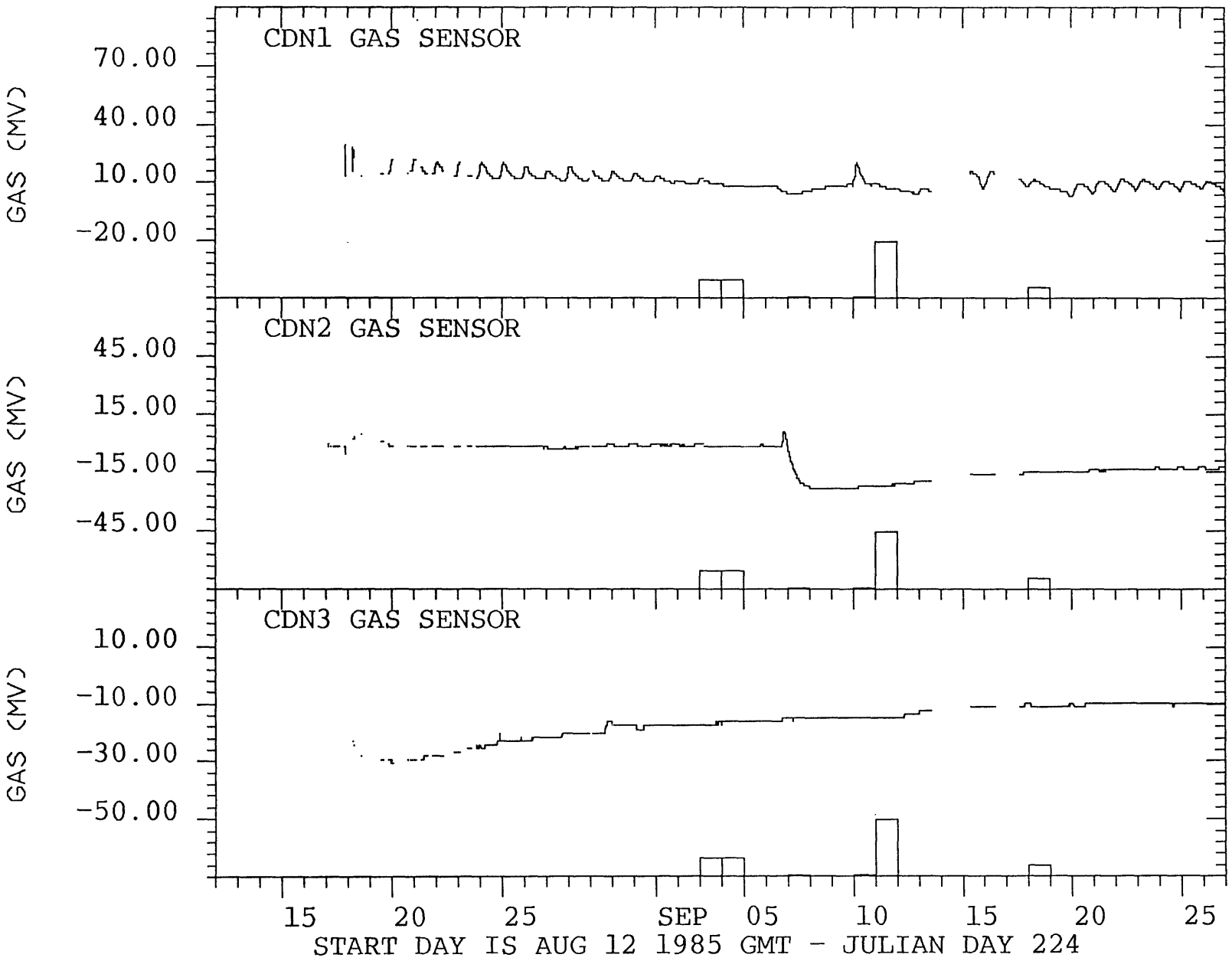
CDN1 GAS SENSOR
70.00
40.00
10.00
-20.00
GAS (MV)
CDN2 GAS SENSOR
45.00
15.00
-15.00
-45.00
GAS (MV)
CDN3 GAS SENSOR
10.00
-10.00
-30.00
-50.00
GAS (MV)
15
20
25
SEP
05
10
15
20
25
START DAY IS AUG 12 1985 GMT - JULIAN DAY 224

FIGURE 24.

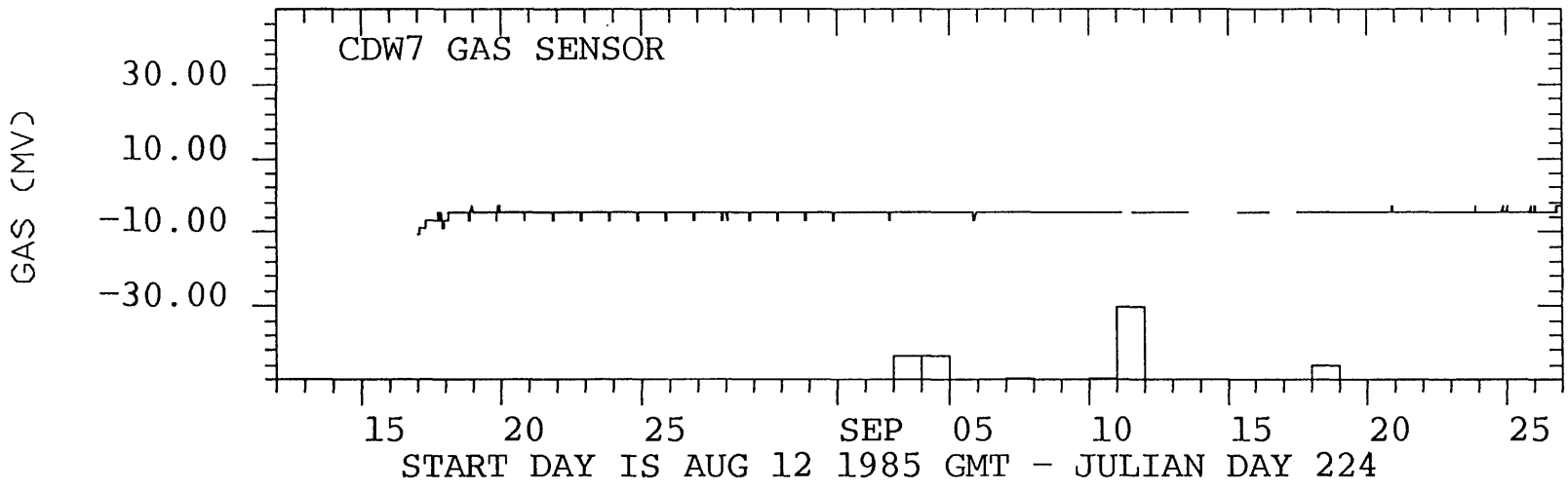
CDW7 GAS SENSOR
GAS (MV)
30.00
10.00
-10.00
-30.00
15
20
25
SEP
05
10
15
20
25
START DAY IS AUG 12 1985 GMT - JULIAN DAY 224

FIGURE 25.

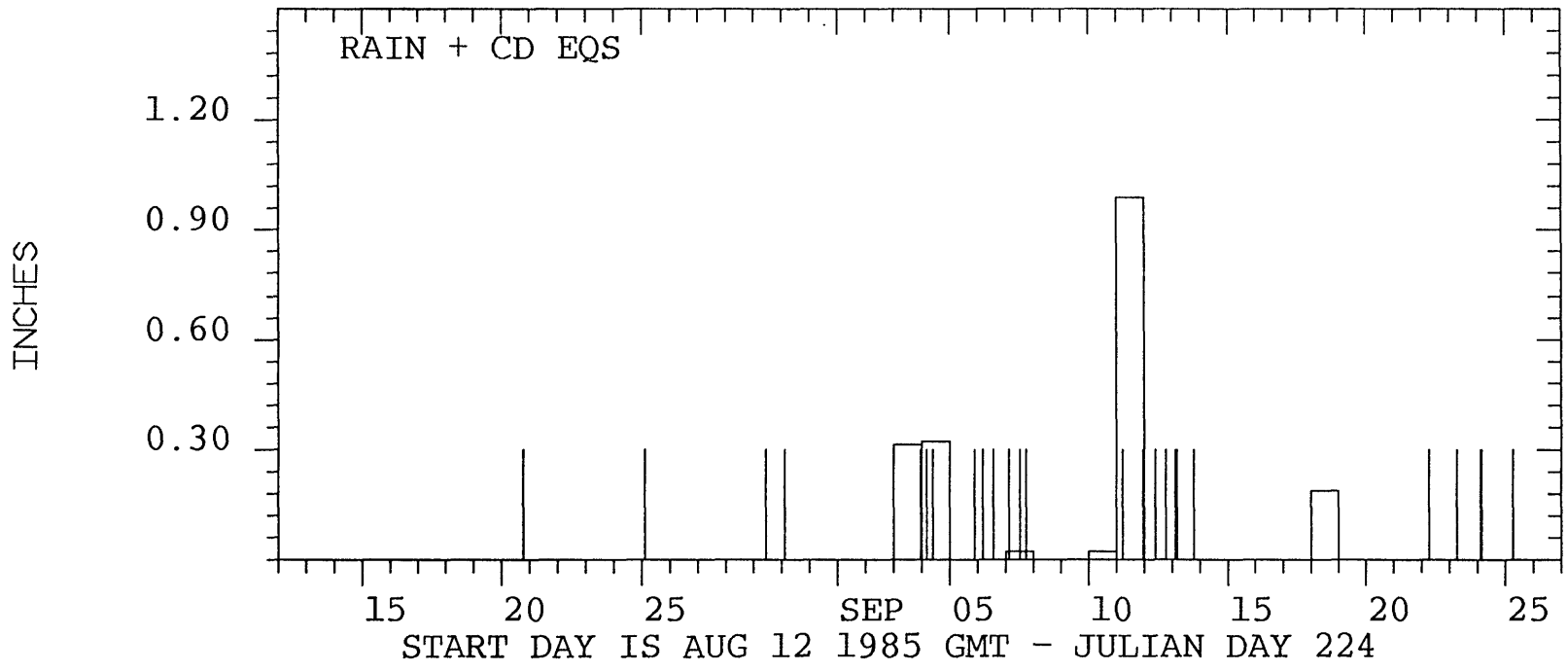
RAIN + CD EQS
INCHES
1.20
0.90
0.60
0.30
15
20
25
SEP
05
10
15
20
25
START DAY IS AUG 12 1985 GMT - JULIAN DAY 224

FIGURE 26.

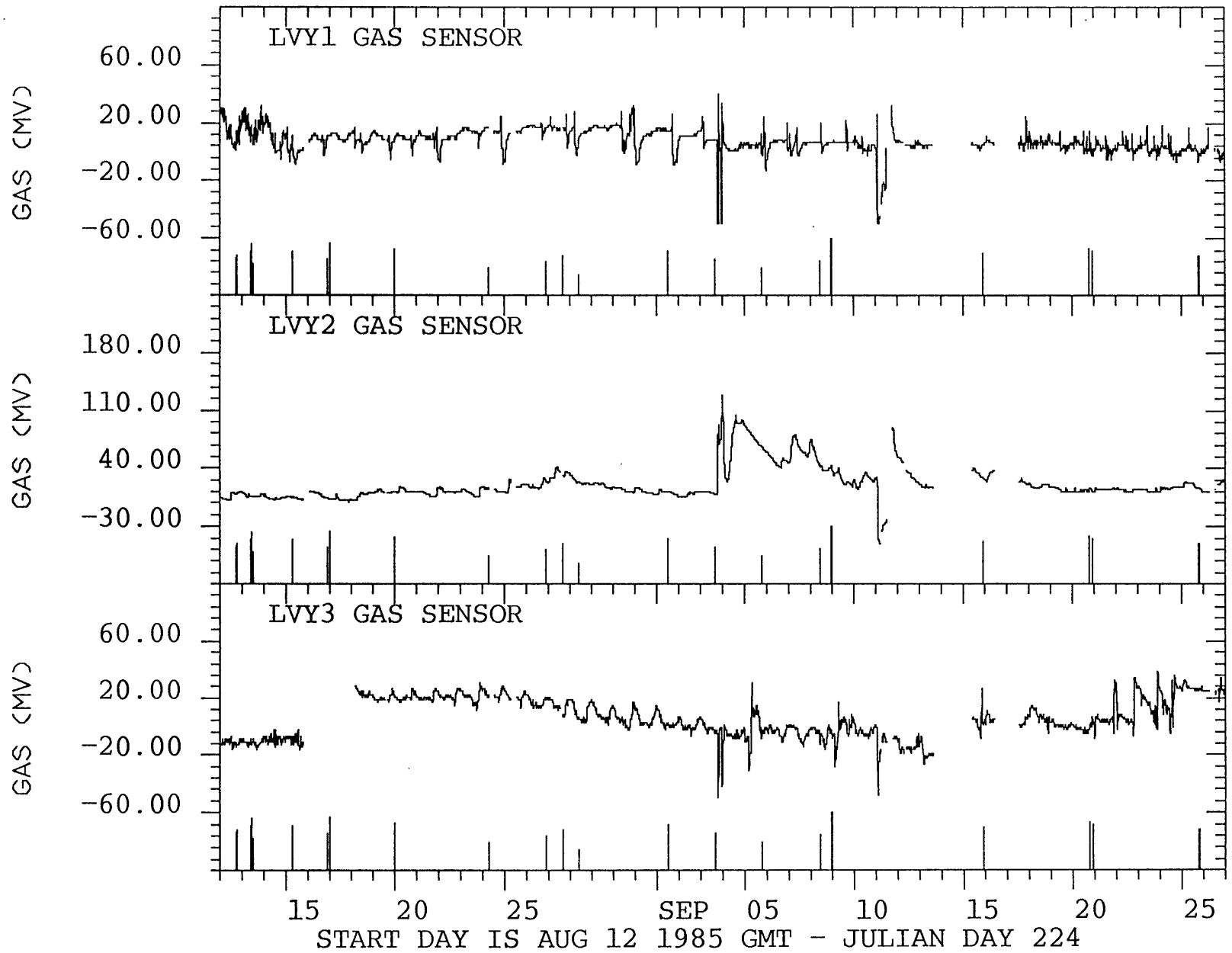
LVY1 GAS SENSOR
60.00
20.00
-20.00
-60.00
GAS (MV)
LVY2 GAS SENSOR
180.00
110.00
40.00
-30.00
GAS (MV)
LVY3 GAS SENSOR
60.00
20.00
-20.00
-60.00
GAS (MV)
15
20
25
SEP
05
10
15
20
25
START DAY IS AUG 12 1985 GMT - JULIAN DAY 224

FIGURE 27.

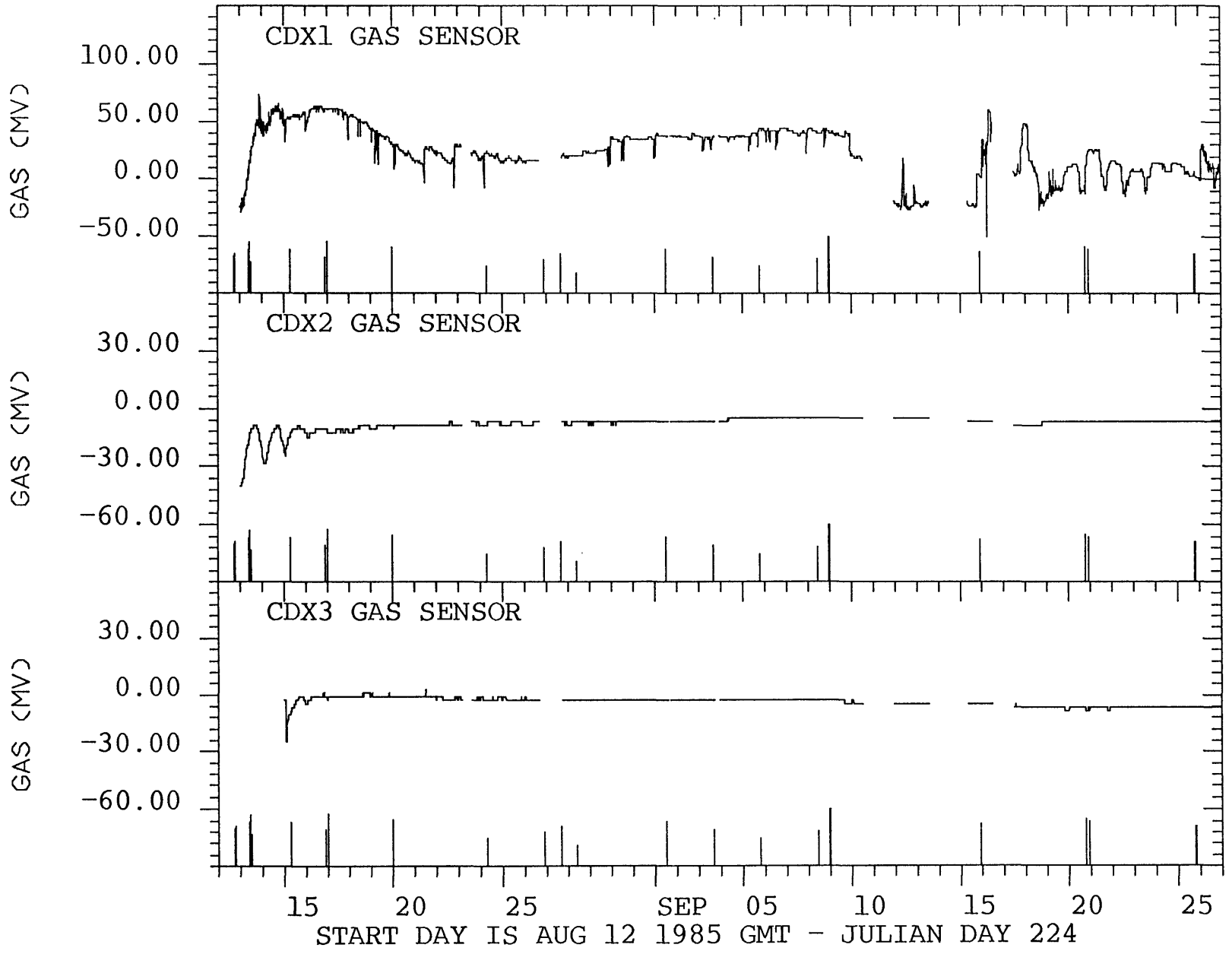
CDX1 GAS SENSOR
100.00
50.00
0.00
-50.00
GAS (MV)
CDX2 GAS SENSOR
30.00
0.00
-30.00
-60.00
GAS (MV)
CDX3 GAS SENSOR
30.00
0.00
-30.00
-60.00
GAS (MV)
15
20
25
SEP
05
10
15
20
25
START DAY IS AUG 12 1985 GMT - JULIAN DAY 224

FIGURE 28.

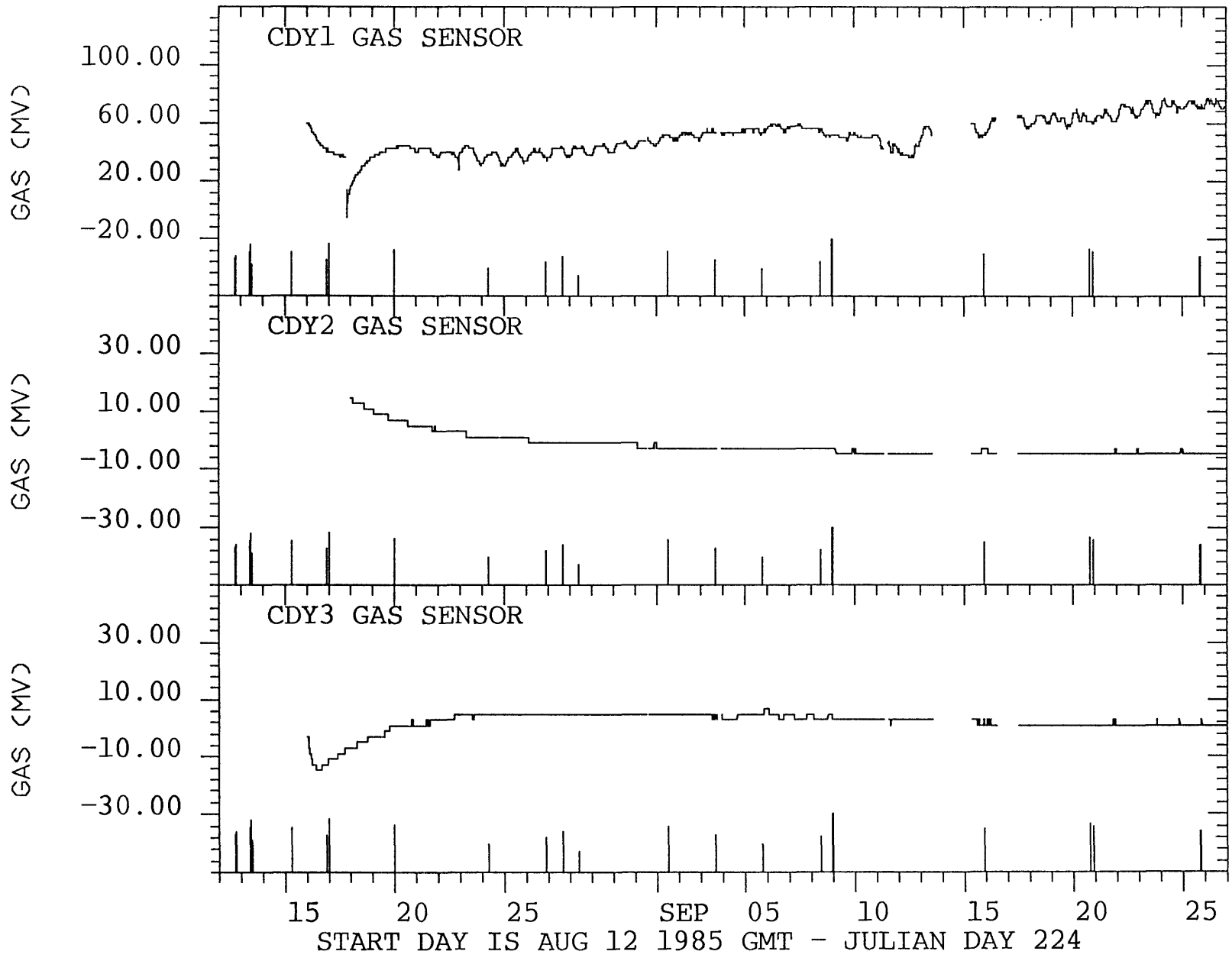
CDY1 GAS SENSOR
100.00
60.00
20.00
-20.00
GAS (MV)
CDY2 GAS SENSOR
30.00
10.00
-10.00
-30.00
GAS (MV)
CDY3 GAS SENSOR
30.00
10.00
-10.00
-30.00
GAS (MV)
15
20
25
SEP
05
10
15
20
25
START DAY IS AUG 12 1985 GMT - JULIAN DAY 224

FIGURE 29.

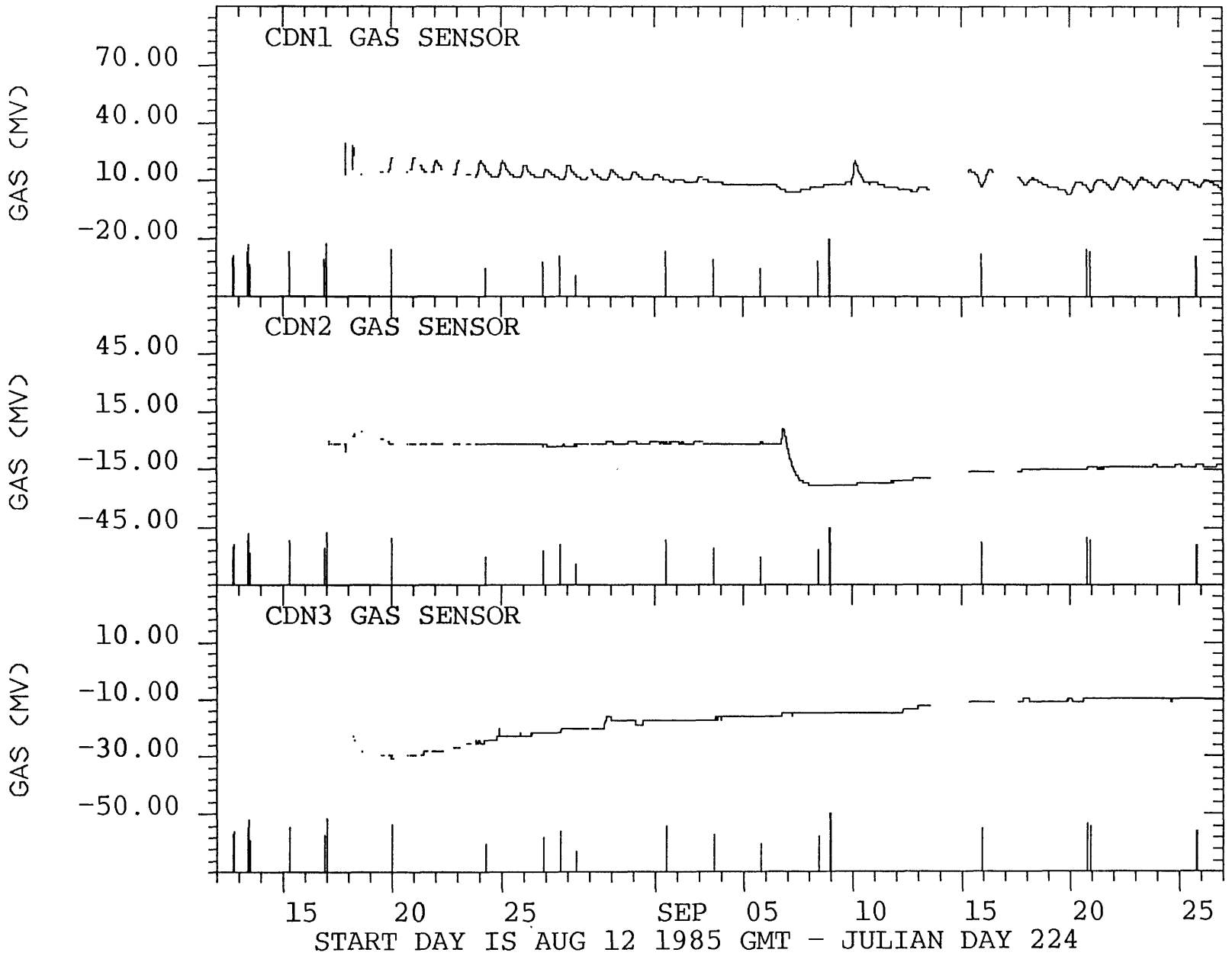
CDN1 GAS SENSOR
70.00
40.00
10.00
-20.00
GAS (MV)
CDN2 GAS SENSOR
45.00
15.00
-15.00
-45.00
GAS (MV)
CDN3 GAS SENSOR
10.00
-10.00
-30.00
-50.00
GAS (MV)
15
20
25
SEP
05
10
15
20
25
START DAY IS AUG 12 1985 GMT - JULIAN DAY 224

FIGURE 30.

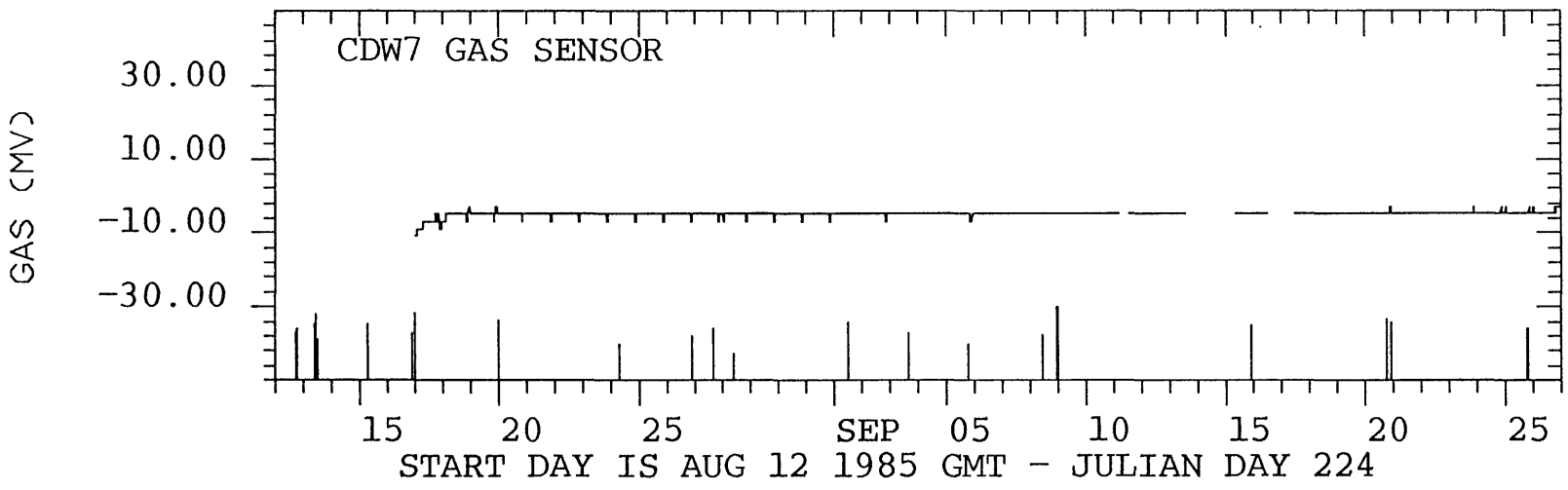
CDW7 GAS SENSOR
GAS (MV)
30.00
10.00
-10.00
-30.00
15
20
25
SEP
05
10
15
20
25
START DAY IS AUG 12 1985 GMT - JULIAN DAY 224

FIGURE 31.

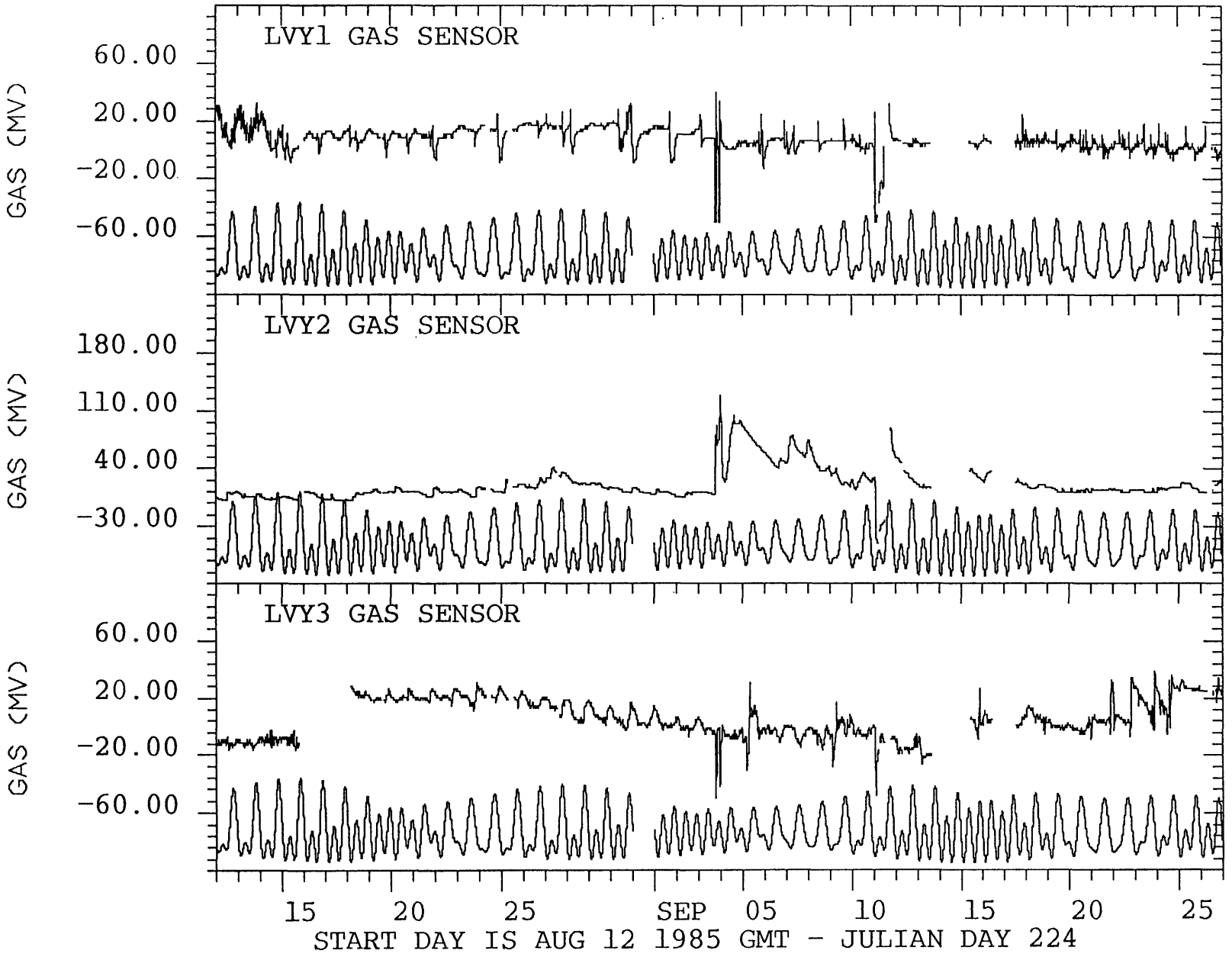
LVY1 GAS SENSOR
60.00
20.00
-20.00
-60.00
GAS (MV)
LVY2 GAS SENSOR
180.00
110.00
40.00
-30.00
GAS (MV)
LVY3 GAS SENSOR
60.00
20.00
-20.00
-60.00
GAS (MV)
15
20
25
SEP
05
10
15
20
25
START DAY IS AUG 12 1985 GMT - JULIAN DAY 224

FIGURE 32.

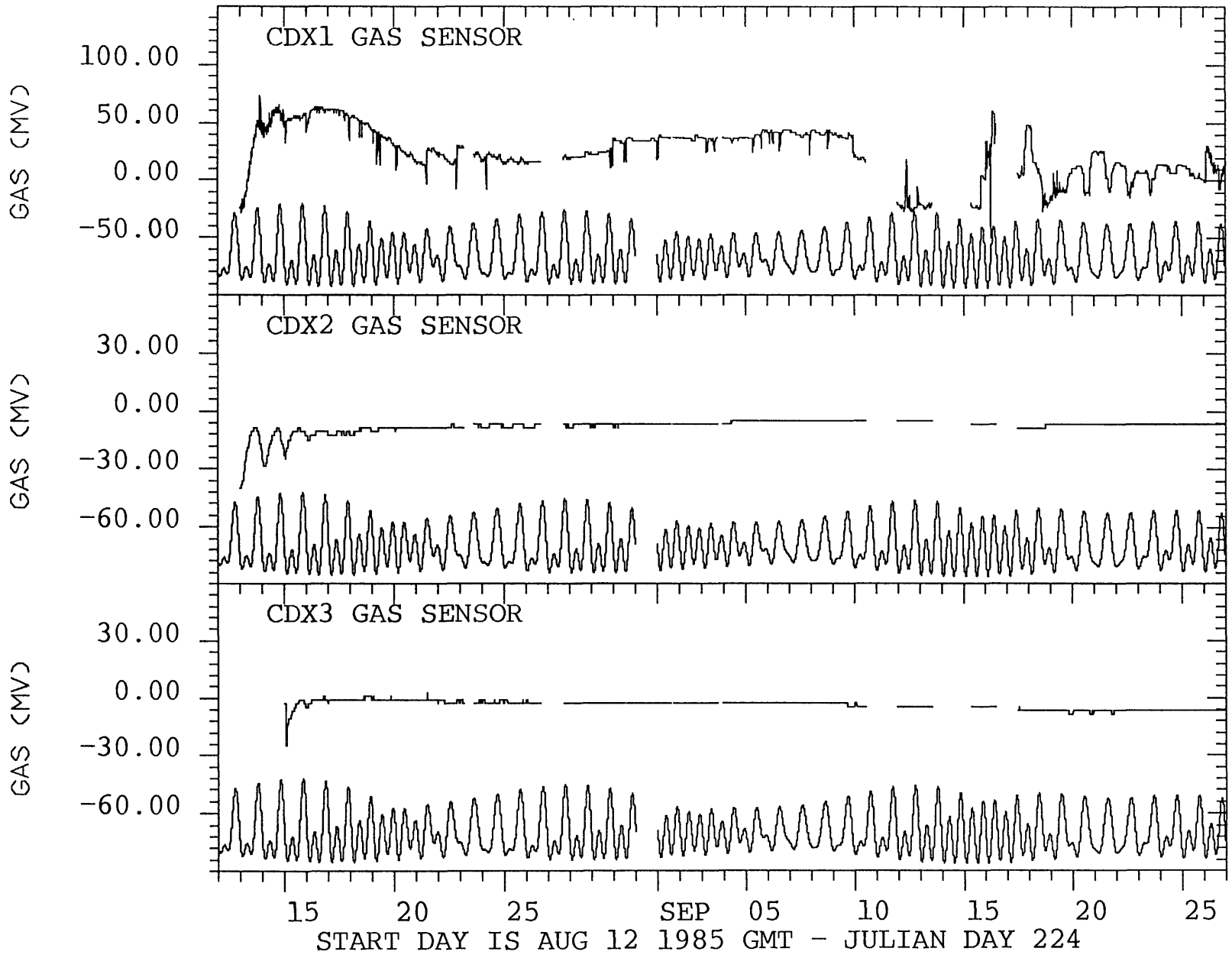
CDX1 GAS SENSOR
100.00
50.00
0.00
-50.00
GAS (MV)
CDX2 GAS SENSOR
30.00
0.00
-30.00
-60.00
GAS (MV)
CDX3 GAS SENSOR
30.00
0.00
-30.00
-60.00
GAS (MV)
15
20
25
SEP
05
10
15
20
25
START DAY IS AUG 12 1985 GMT - JULIAN DAY 224

FIGURE 33.

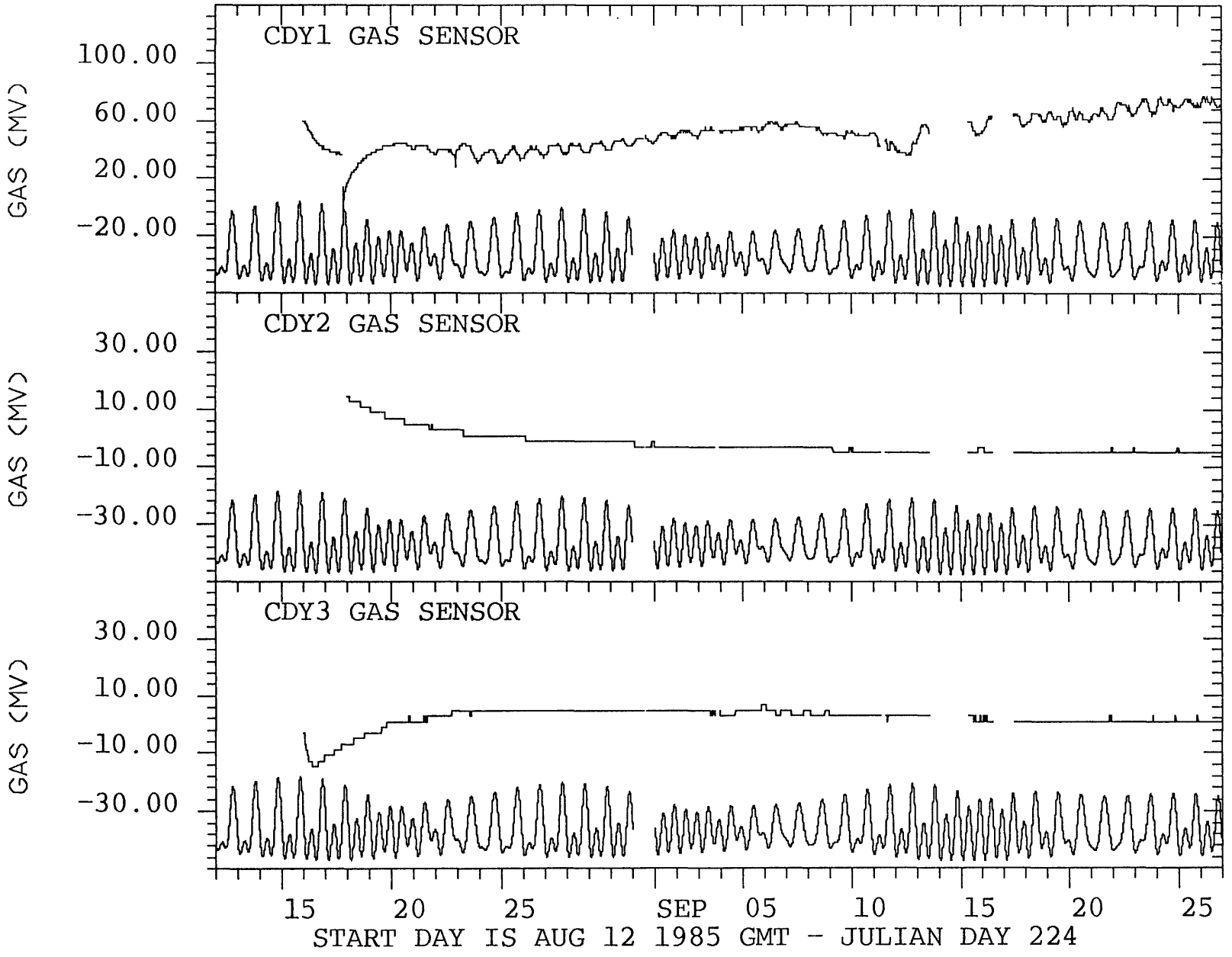
CDY1 GAS SENSOR
100.00
60.00
20.00
-20.00
GAS (MV)
CDY2 GAS SENSOR
30.00
10.00
-10.00
-30.00
GAS (MV)
CDY3 GAS SENSOR
30.00
10.00
-10.00
-30.00
GAS (MV)
15
20
25
SEP
05
10
15
20
25
START DAY IS AUG 12 1985 GMT - JULIAN DAY 224

FIGURE 34.

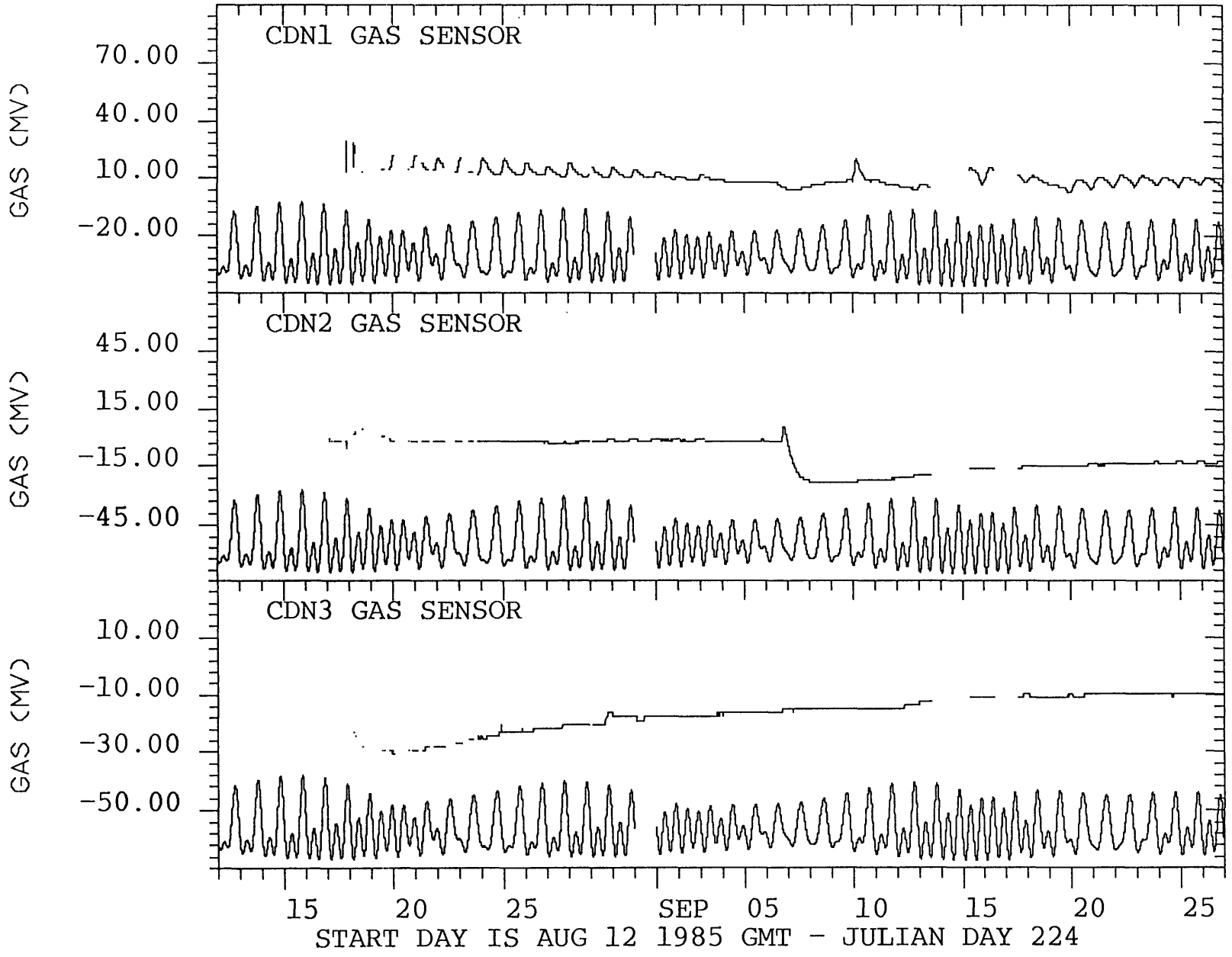
CDN1 GAS SENSOR
70.00
40.00
10.00
-20.00
GAS (MV)
CDN2 GAS SENSOR
45.00
15.00
-15.00
-45.00
GAS (MV)
CDN3 GAS SENSOR
10.00
-10.00
-30.00
-50.00
GAS (MV)
15
20
25
SEP
05
10
15
20
25
START DAY IS AUG 12 1985 GMT - JULIAN DAY 224

FIGURE 35.

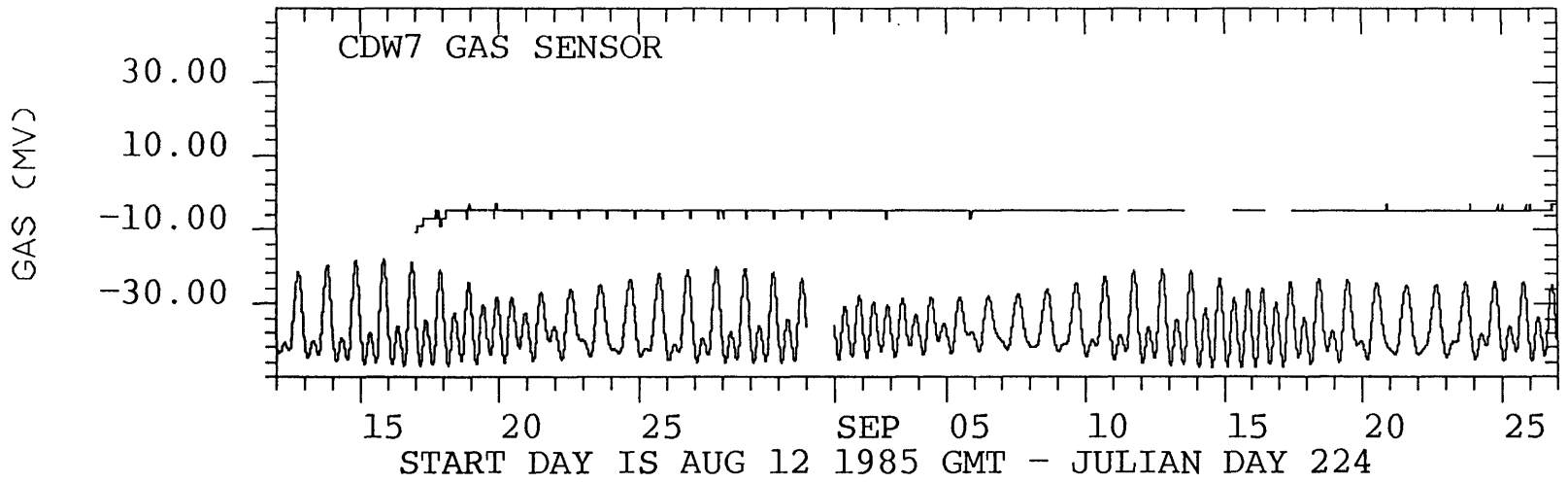
CDW7 GAS SENSOR
GAS (MV)
30.00
10.00
-10.00
-30.00
15
20
25
SEP
05
10
15
20
25
START DAY IS AUG 12 1985 GMT - JULIAN DAY 224

FIGURE 36.

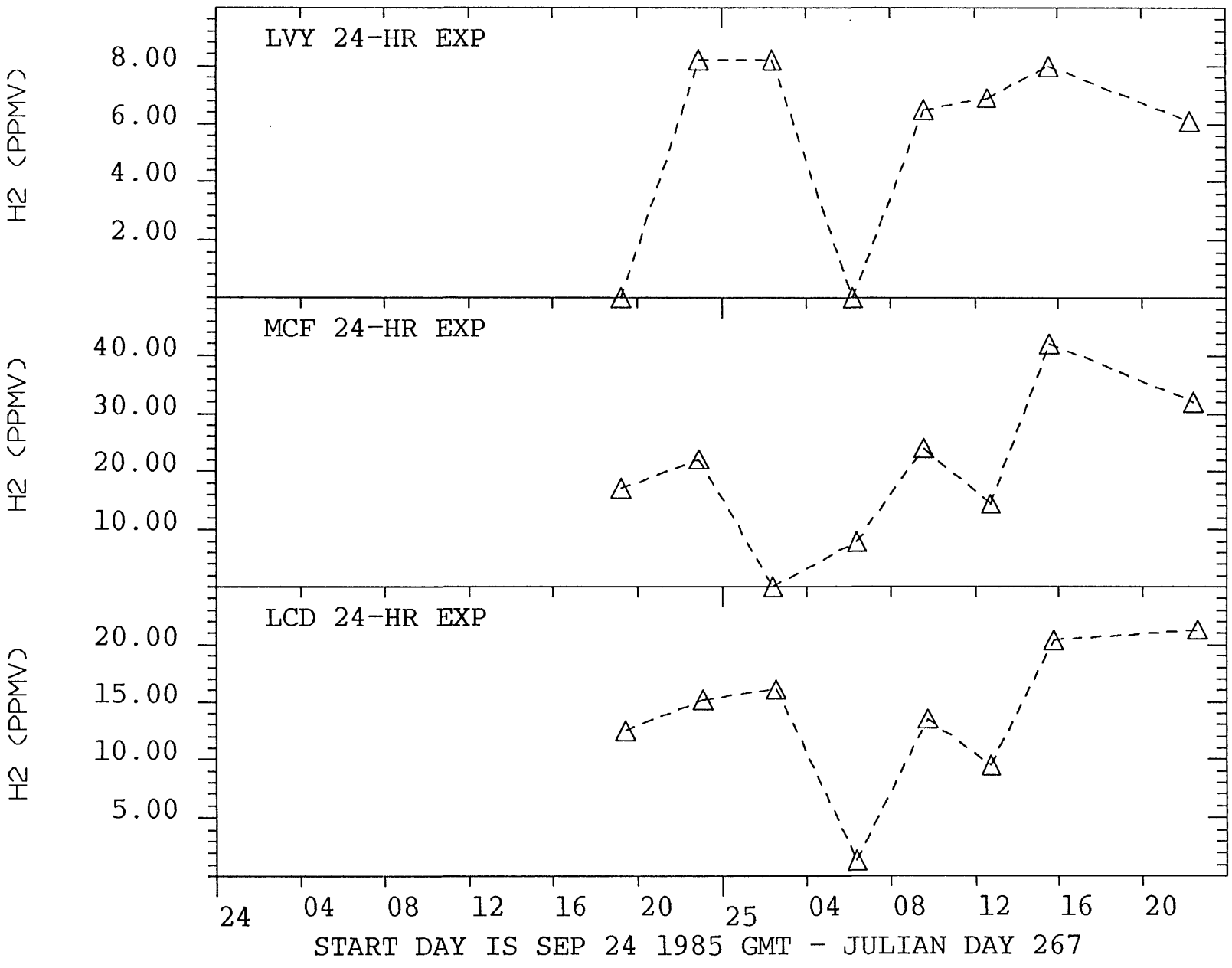
LVY 24-HR EXP
8.00
6.00
4.00
2.00
H2 (PPMV)
MCF 24-HR EXP
40.00
30.00
20.00
10.00
H2 (PPMV)
LCD 24-HR EXP
20.00
15.00
10.00
5.00
H2 (PPMV)
24
04
08
12
16
20
25
04
08
12
16
20
START DAY IS SEP 24 1985 GMT - JULIAN DAY 267

FIGURE 37.

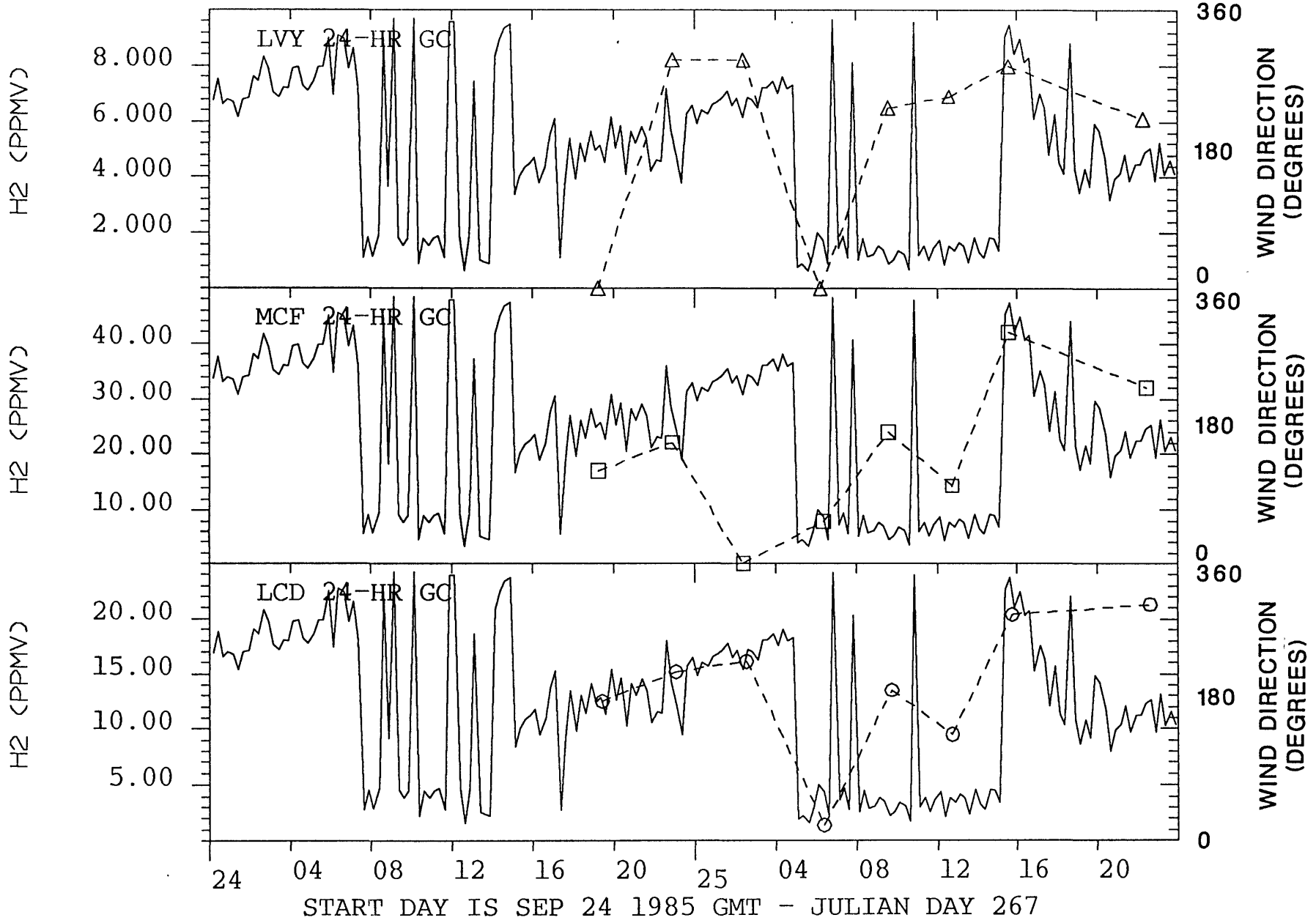
LVY 24-HR GC
MCF 24-HR GC
LCD 24-HR GC
H2 (PPMV)
8.000
6.000
4.000
2.000
40.00
30.00
20.00
10.00
15.00
5.00
WIND DIRECTION (DEGREES)
360
180
0
24
04
08
12
16
20
25
START DAY IS SEP 24 1985 GMT - JULIAN DAY 267

FIGURE 38.

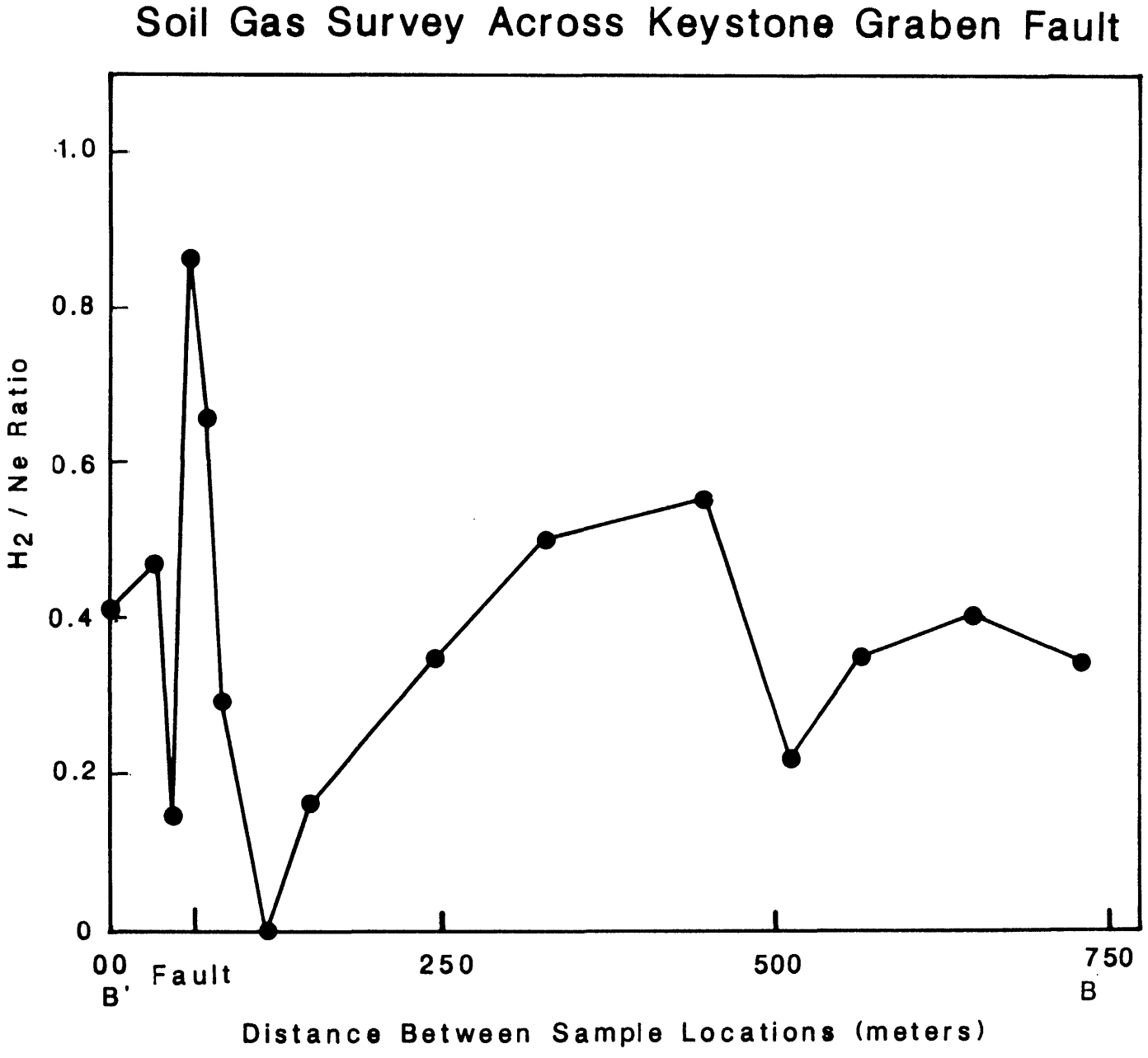
Soil Gas Survey Across Keystone Graben Fault
1.0
0.8
0.6
0.4
0.2
0
H2 / Ne Ratio
00
B'
Fault
250
500
750
B
Distance Between Sample Locations (meters)

FIGURE 39.

FIGURE 38. Plot showing recorded wind direction data superimposed on the analyzed hydrogen content of fumaroles LVY, MCF, and LCD for a 24-hour period beginning September 24, 1985. The vertical scale for wind direction is 0 to 360 compass degrees, the direction from which the wind is blowing. Notice that the minimum values for hydrogen occur near the time of the shift of the orographic winds from upslope to downslope and that the maximum values for hydrogen occur in the morning near the time when the winds shift back to upslope.

FIGURE 39. Plot showing the hydrogen/neon ratio of analyzed soil gas samples taken along traverse B - B' across the eastern keystone graben fault suggesting a structural control for degassing.